Eksperimentalni model prirodne ventilacije zgrade u urbanoj sredini

Golubić, Dino

Master's thesis / Diplomski rad

2018

Degree Grantor / Ustanova koja je dodijelila akademski / stručni stupanj: **University of Zagreb, Faculty of Mechanical Engineering and Naval Architecture / Sveučilište u Zagrebu, Fakultet strojarstva i brodogradnje**

Permanent link / Trajna poveznica: https://urn.nsk.hr/urn:nbn:hr:235:996809

Rights / Prava: In copyright/Zaštićeno autorskim pravom.

Download date / Datum preuzimanja: **2024-12-24**

Repository / Repozitorij:

Repository of Faculty of Mechanical Engineering and Naval Architecture University of Zagreb

UNIVERSITY OF ZAGREB

Faculty of Mechanical Engineering and Naval Architecture

MASTER THESIS

Dino Golubić

Zagreb, 2018

UNIVERSITY OF ZAGREB

Faculty of Mechanical Engineering and Naval Architecture

EXPERIMENTAL MODEL OF BUILDING NATURAL VENTILATION IN URBAN ENVIRONMENT

Mentors: Student:

Prof. Hrvoje Kozmar, PhD   Dino Golubić

Ass. Prof. Walter Meile, PhD

Zagreb, 2018

I hereby declare that this thesis is entirely the result of my own work except where otherwise indicated. I have fully cited all used sources and only used the ones given in the list of references.

Dino Golubić

ACKNOWLEDGMENTS

Sveučilište u Zagrebu	
Fakultet strojarstva i brodogradnje	
Datum	Prilog
Klasa:	
Ur. broj:	

DIPLOMSKI ZADATAK

Student: **Dino Golubić**   Mat. br.: 0035190559

Naslov rada na
hrvatskom jeziku: **Eksperimentalni model prirodne ventilacije zgrade u urbanoj sredini**

Naslov rada na
engleskom jeziku: **Experimental model of building natural ventilation in urban environment**

Opis zadatka:

Natural ventilation of buildings is one of the most important aspects for a good indoor air quality. The basic ventilation parameter is the air change rate (ACH), which represents the air removed from an indoor space divided by the indoor space volume. ACH strongly depends on wind characteristics in the lower atmosphere, as well as on the openness of building doors and windows. Building position in the urban environment with various spacing densities and heights of buildings is a key factor for the ACH calculation.

In this study, wind-tunnel experiments on the influence of the spacing density of buildings on the ACH will be performed in a boundary layer wind tunnel of the Institute of Fluid Mechanics and Heat Transfer at the Graz University of Technology, Austria. The cubic building model with two window openings will be studied in a stand-alone configuration, as well as a part of an urban neighborhood. The air transport through the windows will be measured using the Tracer Gas System for a stand-alone cubic building model, as well as for a building model as a part of the urban-neighborhood model with various spacing densities of buildings in the urban-neighborhood model. The effects of various flow incidence angles and velocities will be studied.

In this thesis, it is necessary to provide:
1) Introduction including theoretical background on aerodynamics of buildings and their natural ventilation;
2) Experimental setup including details of the wind-tunnel design, simulation of the atmospheric boundary layer, experimental technique and procedure;
3) Results and discussion;
4) Conclusions.

It is advised to list references used in this work, as well as to acknowledge help and support received during this study.

Zadatak zadan: Datum predaje rada: Predviđeni datum obrane:

18. siječnja 2018.   22. ožujka 2018.   28., 29. i 30. ožujka 2018.

Zadatak zadao: Predsjednica Povjerenstva:

Prof. dr. sc. Hrvoje Kozmar

Ass. Prof. Dr. techn. Walter Meile   Prof. dr. sc. Tanja Jurčević Lulić

Table of Contents

List of Figures

List of Tables

Nomenclature

Greek letters

α	Power-law exponent	-
β	Flow incidence angle	°
δ	Boundary layer thickness	m
κ	von Kármán constant	-
ω	Angular velocity	rad/s
ϕ	Angle of latitude	°
Φ_{conv}	Convective heat flux	W
ρ	Density	kg/m^3
τ	Reynolds shear stress	N/m^2

Latin letters

$\dot{m}$	Mass flow rate	kg/s
$\dot{V}$	Volume flow rate	m^3/s
$\mathbf{n}$	Normal unit vector	-
$\bar{u}, \bar{v}, \bar{w}$	Mean velocity in the x-, y- and z- direction	m/s
A	Surface area	m^2
C	Tracer gas mass concentration	-
C_D	Discharge coefficient	-
c_F	Dimensionless force coefficient	-
C_v	Effectiveness of opening	-
c_w	Specific heat of the hot-wire sensor	J/kgK
d	Displacement height	m
E	Mass injection rate	kg/s
f	Coriolis parameter	1/s

F_c	Coriolis force	N
I_u, I_v, I_w	Turbulence intensity in the x-, y- and z- direction	-
I_w	Electric current intensity	A
k_w	Eddy wave number	-
L_u^x, L_u^y, L_u^z	Longitudinal integral length scale of turbulence in the x-, y- and z- direction	m
m	Mass	kg
p	Pressure	Pa
R_u^x	Correlation coefficient	-
R_w	Resistance of the hot-wire sensor	Ω
S_u	Power spectral density of longitudinal velocity fluctuations	m^2/s^2
T	Acquisition time	s
t	Time	s
T_a	Unheated wire temperature	°C
T_w	Heated wire temperature	°C
u', v', w'	Fluctuating velocity component in the x-, y- and z- direction	m/s
u, v, w	Absolute velocity in the x-, y- and z- direction	m/s
u_δ	Flow velocity at the top of the boundary layer	m/s
u_τ	Friction velocity	m/s
V	Volume	m^3
y_C	Distance in the lateral direction, middle of the cross section	m
y_L	Distance in the lateral direction, left-hand side downstream	m
y_R	Distance in the lateral direction, right-hand side downstream	m
z	Vertical distance	m
z_0	Aerodynamic surface roughness length	m
$z_{0,m}$	Model aerodynamic surface roughness length	m

$z_{0,p}$ Prototype aerodynamic surface roughness length   m

z_{ref} Reference height   m

ACH   Air change rate h^{-1}

Abstract

Natural ventilation is the process of air change in an indoor space without using mechanical devices, i.e by using simply natural forces like flow momentum and buoyancy. When designing bioclimatic, passive, high performance buildings, it is important to enhance natural ventilation in order to minimize energy consumption, improve air quality and reduce environmental pollution. The scope of the present work is on a sensitivity of ventilation rates for a building, which is a part of an urban neighborhood. The cross-ventilation and single-side ventilation for various flow incidence angles were studied. Measured ventilation rates were compared to the reference results that were obtained for a referent stand-alone cubic building model. The experiments were carried out in the atmospheric boundary layer wind tunnel at the Institute of Fluid Mechanics and Heat Transfer (IFMHT) at the Graz University of Technology (GUT), Austria. The hot-wire anemometry was used to determine flow characteristics, while the tracer gas system was applied to estimate airflow rates of the cubic building model. The atmospheric boundary layer was successfully simulated for a suburban terrain exposure. The airflow rates obtained for a ventilation of a stand-alone cubic building model were observed to be larger when compared to a cubic building model situated in an urban neighborhood model. In the latter case, the ventilation efficiency is larger for less densely spaced building models.

Keywords: *natural ventilation*, *atmospheric boundary layer*, *urban environment*, *small-scale experiments*, *atmospheric boundary layer wind tunnel*

Sažetak

Prirodna ventilacija je proces izmjene zraka iz zgrada bez uporabe ventilacijskih uređaja, npr. koristeći količinu gibanja zraka i uzgonske sile. Pri izradi bioklimatskih zgrada visokih performansi veliki je naglasak na povećanju učinka prirodne ventilacije kako bi se smanjila potrošnja energije, poboljšala kvaliteta zraka te smanjila onečišćenja okoliša. Predmet ovog rada jest određivanje odnosa intenziteta ventilacije zgrade za samostojeću zgradu, kao i za zgradu smještenu u urbanom okruženju za različite stupnjeve izgrađenosti. Ispitivani su utjecaji poprečne i jednostrane ventilacije i smjera strujanja zraka. Izmjerene brzine ventilacije uspoređene su s rezultatima dobivenim za izoliranu referentnu zgradu. Eksperimenti su provedeni u zračnom tunelu za generiranje modela atmosferskog graničnog sloja na Institutu za mehaniku fluida i prijenos topline Tehničkog sveučilišta u Grazu, Austrija. Za određivanje karakteristika strujanja zraka je korišten sustav užarene žice, dok je sustav praćenja plina korišten za mjerenje broja izmjena zraka u prostoriji. Atmosferski granični sloj je uspješno modeliran za strujanje zraka iznad suburbanog tipa terena. Izmjena zraka za samostojeću zgradu je znatno efikasnija u odnosu na zgradu smještenu unutar urbanog okruženja. Za slučaj urbanog okruženja, efikasnost ventilacije zgrade je veća za slučaj rjeđe raspoređenih zgrada.

Ključne riječi: *prirodna ventilacija*, *atmosferski granični sloj*, *urbano okruženje*, *modelski eksperimenti*, *zračni tunel za simulaciju atmosferskog graničnog sloja*

Prošireni Sažetak (Extended Abstract in Croatian)

Uvod

Prirodna ventilacija je proces izmjene zraka u prostoriji bez uporabe mehaničkih uređaja. Prednosti ovakvog tipa ventilacije su mali investicijski troškovi, jeftina pogonska energija, poboljšana kvaliteta zraka i smanjenje onečišćenja. Prirodna ventilacija se dijeli na ventilaciju uzrokovanu razlikom tlaka između prostorije i okoliša, te ventilaciju uzrokovanu temperaturnim razlikama. Predmet ovog rada je isključivo ventilacija uzrokovana razlikom tlaka.

U gusto naseljenim urbanim područjima, gdje gusto smještene zgrade bitno utječu na strujanje i mijenjaju polje tlaka zraka, učinkovitost prirodne ventilacije je smanjena. Raspored i razmak među zgradama imaju ključnu ulogu u omogućavanju optimalne ventilacije kako bi se osigurali povoljni životni uvjeti.

Cilj ovog rada jest eksperimentalno ispitati intenzitet prirodne ventilacije zgrade u ovisnosti o razmaku prema susjednim zgradama urbane četvrti. Broj izmjena zraka u prostoriji prvotno je određen za izolirani model zgrade s dva prozora. Potom je uvedeno dodatnih osam eksperimentalnih konfiguracija kako bi se simulirali uvjeti urbane četvrti. U oba slučaja, mjerenja su prvotno provedena s oba otvorena prozora (poprečna ventilacija), a potom samo s jednim otvorenim prozorom (jednostrana ventilacija).

Karakteristike atmosferskog graničnog sloja i prirodne ventilacije

Dio troposfere unutar kojeg na strukturu strujanja zraka utječe površina Zemlje se naziva atmosferski granični sloj. U atmosferskom graničnom sloju, vrijednosti brzine strujanja zraka su na podlozi jednake nuli i rastu do maksimuma na rubu graničnog sloja δ. Približna debljina atmosferskog graničnog sloja iznosi između 450 i 600 m [2], te se sastoji od vanjskog i unutarnjeg sloja. U vanjskom sloju strujanje je neovisno o karakteristikama terena te Coriolisova sila uslijed rotacije Zemlje ima značajnu ulogu. Unutarnji sloj se sastoji od inercijalnog i prijelaznog podsloja, a strujanje uvelike ovisi o hrapavosti podloge i neovisno je o rotaciji Zemlje.
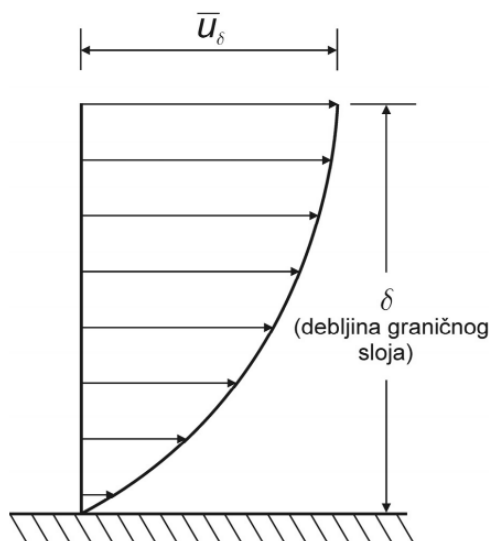
Slika I: Atmosferski granični sloj, [3]

Strujanje zraka unutar atmosferskog graničnog sloja je turbulentno. Najznačajniji parametri koji opisuju karakteristike atmosferske turbulencije su intenzitet turbulencije, integralna duljinska mjera turbulencije, spektar kinetičke energije turbulentnih pulzacija brzine i Reynoldsovo naprezanje.

Prirodna ventilacija označuje proces opskrbe i uklanjanja zraka iz unutrašnjeg prostora isključivo putem prirodnih sila. Učinkovitost ventilacije opisuje se brojem izmjena zraka (ACH) unutar prostorije u jednom satu:

$$\text{ACH} = \frac{\dot{V}}{V_R},\tag{1}$$

gdje je V_R volumen promatrane prostorije, a $\dot{V}$ volumni protok.

Eksperimentalne postavke

Eksperimenti su provedeni u zračnom tunelu za generiranje modela atmosferskog graničnog sloja na Institutu za mehaniku fluida i prijenos topline Tehničkog sveučilišta u Grazu, Austrija. Za simulaciju donjeg dijela atmosferskog graničnog sloja korištena je rešetka cilindričnih štapova, nazubljena barijera te elementi podne hrapavosti. Mjerenja brzine provedena su tehnikom užarene žice, dok je za mjerenje ventilacije korišten sustav praćenja plina. Prirodna ventilacija ispitivana je na pojednostavljenom modelu zgrade s dva poprečno postavljena otvora, Slika II.
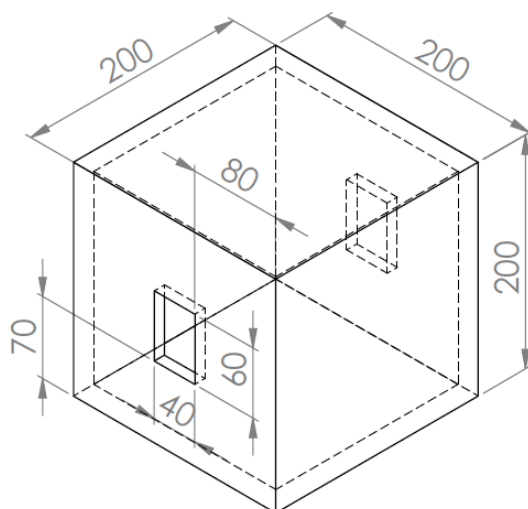
Slika II: Ispitivani model zgrade, jedinice su dane u mm

Urbana četvrt prikazana je s osam dodatnih modela zgrade u 3 x 3 kvadratnom rasporedu, Slika III. Broj izmjena zraka u središnjem modelu zgrade mjeren je za tri različita slučaja:

    a)   Mala udaljenost između modela, $d = 0.5a$, gdje je a dužina brida modela ($a = 200$ mm),

    b)   Srednja udaljenost između modela, $d = a$,

    c)   Velika udaljenost između modela, $d = 1.5a$.
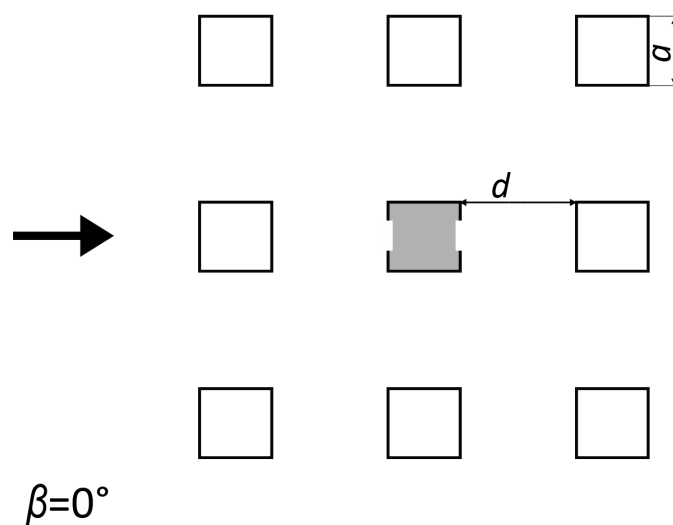
Slika III: Ispitivana konfiguracija za mjerenje poprečne ventilacije u urbanoj četvrti

Rezultati i zaključak

Usporedbe profila osrednjenih vrijednosti brzine sa zakonom potencije i logaritamskim zakonom prikazane su Slikom IV.

a)   b)
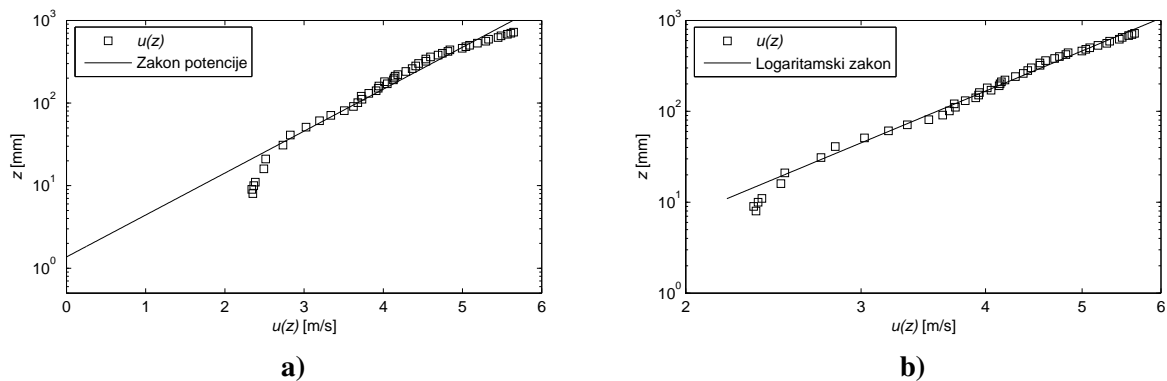
Slika IV: Usporedba profila osrednjenih vrijednosti brzine strujanja zraka sa zakonom potencije a) i logaritamskim zakonom b)

Eksperimentalni rezultati prikazani su kao intenzitet turbulencije, integralne duljinske mjere turbulencije i spektralna raspodjela kinetičke energije, Slike V i VI.

a)   b)
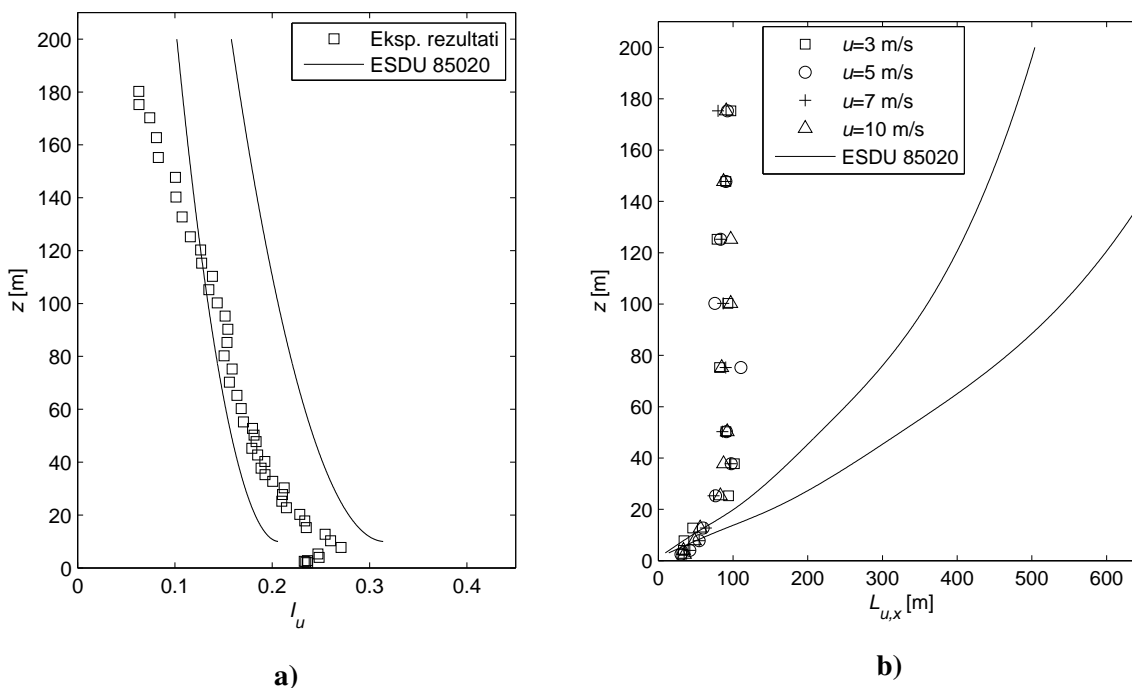
Slika V: Usporedba intenziteta turbulencije a) i integralnih duljinskih mjera turbulencije b) s međunarodnim standardom ESDU 85020
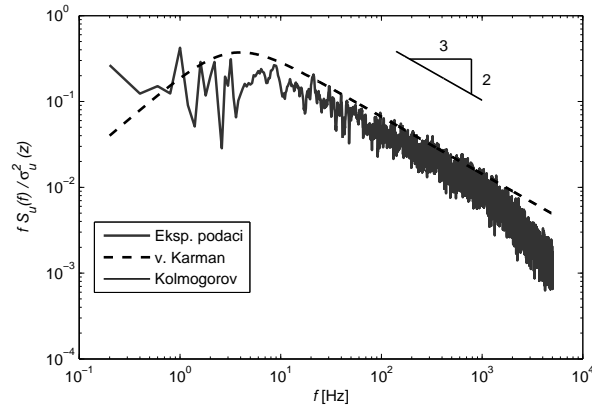
Slika VI: Usporedba spektralne raspodjele kinetičke energije turbulencije s teorijskim modelima von Kármána i Kolmogorova

Za slučaj izolirane zgrade, ovisnost broja izmjena zraka u prostoriji i kuta nastrujavanja prikazana je Slikom VII.

a)   b)
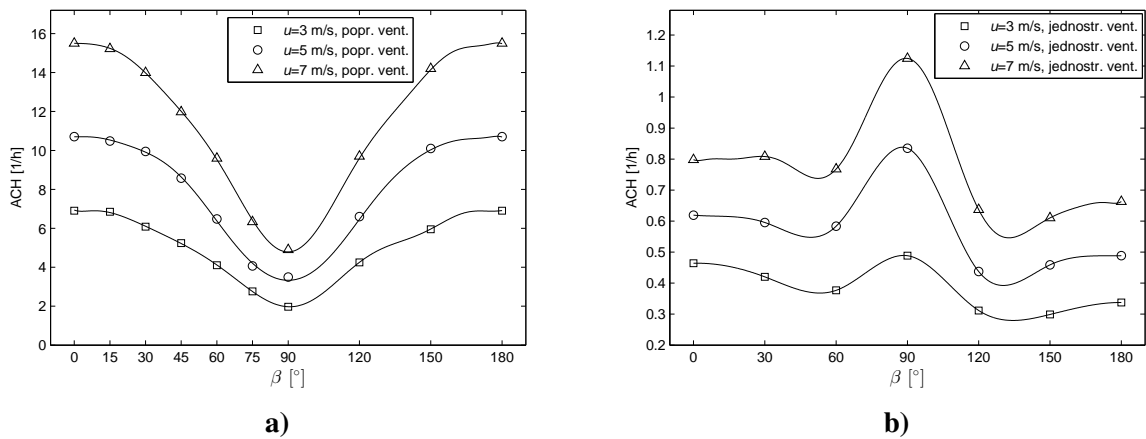
Slika VII: Ovisnost broja izmjena zraka o kutu nastrujavanja izolirane zgrade, za poprečnu a) i jednostranu b) ventilaciju

Rezultati izmjereni za slučaj promatrane zgrade u urbanoj četvrti prikazani su Slikama VIII i IX.

a)

b)

c)
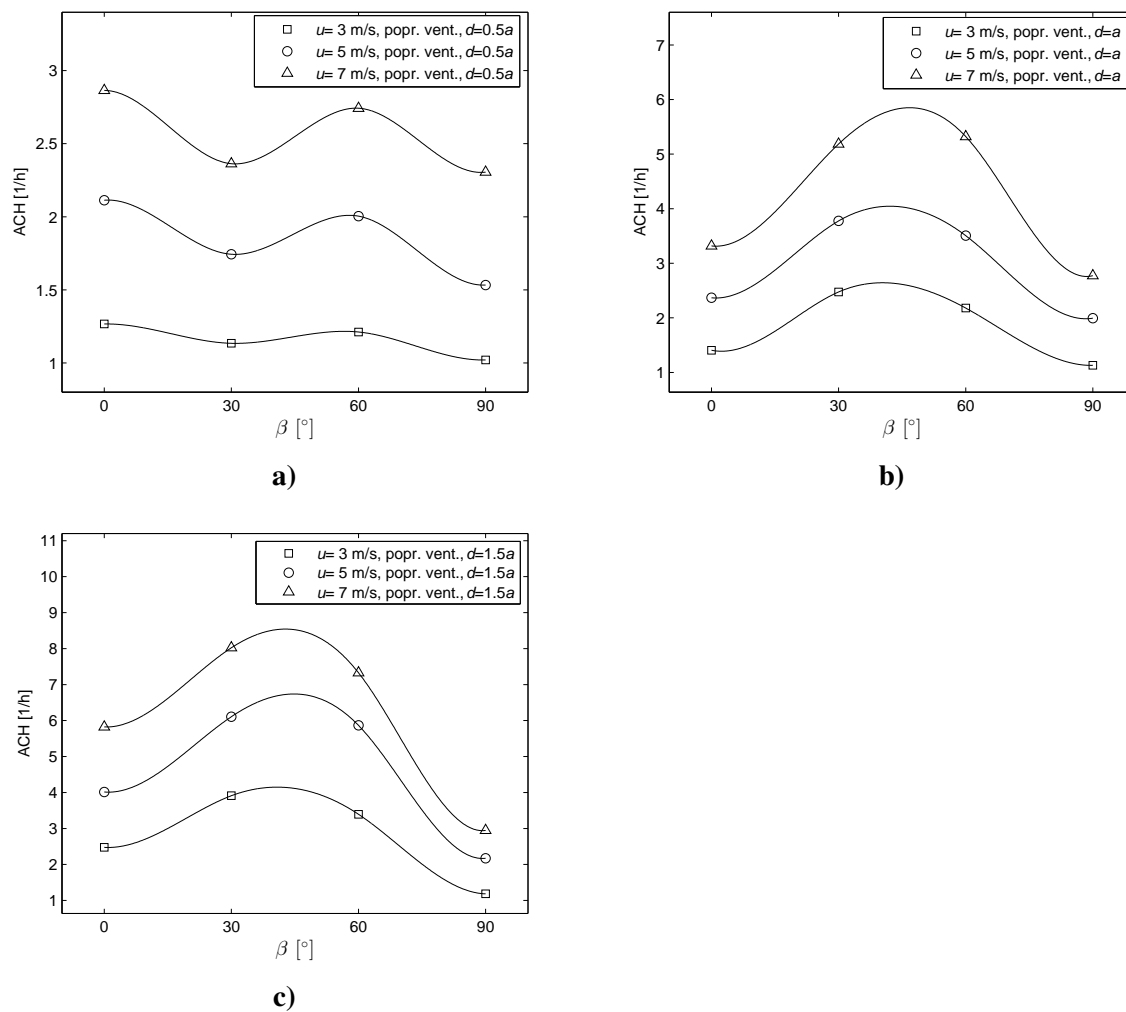
Slika VIII: Ovisnost broja izmjena zraka o kutu nastrujavanja za poprečno ventiliranu zgradu u urbanoj četvrti, slučajevi: a) $d = 0.5a$;   **b)** $d = a$;   **c)** $d = 1.5a$
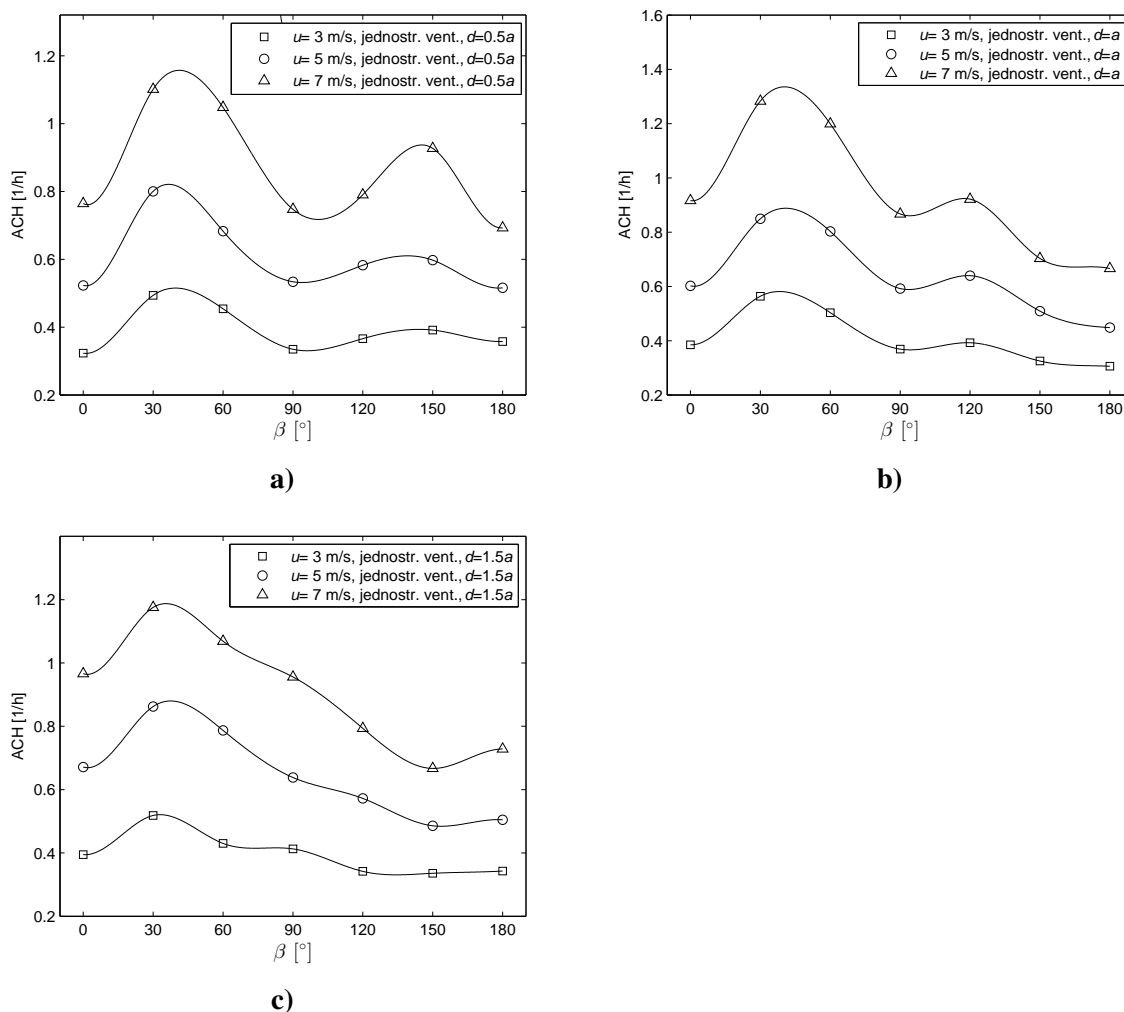
Slika IX: Ovisnost broja izmjena zraka o kutu nastrujavanja za jednostrano ventiliranu zgradu u urbanoj četvrti, slučajevi: a) $d = 0.5a$;   **b)** $d = a$;   **c)** $d = 1.5a$

Uspješno je modeliran atmosferski granični sloj karakterističan za prigradski tip terena. Profili osrednjenih brzina dobro se podudaraju sa zakonom potencije ($\alpha = 0.22$) te logaritamskim zakonom. Intenzitet turbulencije u dobroj je suglasnosti s međunarodnim standardom ESDU 85020, dok se vrijednosti integralnih duljinskih mjera turbulencije podudaraju s ESDU 85020 samo u području blizu površine, a u slojevima iznad ostaju konstantne što nije u skladu s ESDU podacima. Spektralna raspodjela kinetičke energije turbulencije eksperimentalnih rezultata se podudara s teorijskim modelima von Kármána i Kolmogorova.

Poprečno ventilirana i izolirana zgrada postiže najveći broj izmjena zraka za kut nastrujavanja $\beta = 0°$, dok se jednostrano ventilirana zgrada najbolje ventilira pri $\beta = 90°$. Za poprečno ventiliranu zgradu u urbanoj četvrti učinkovitost ventilacije raste s povećanjem razmaka među zgradama. S druge strane, kod jednostrane ventilacije, za određene kuteve nastrujavanja i razmake između zgrada, nepovoljan utjecaj okolnih zgrada nestaje i dolazi do pozitivnog utjecaja okolnih zgrada na ventilaciju.

1   Introduction

Natural ventilation is the process of air exchange in indoor spaces in order to allow for passive cooling and ventilation. Its use is definitely an advantage in light of the raising concerns regarding the costs, environmental impact and health regulations. When carefully designed, natural ventilation can reduce building operation costs and reduce the energy consumption for air-conditioning and circulating fans. Martin and Fitzsimmons [4] reported a reduction in capital cost up to 15% by incorporating natural ventilation systems in buildings. Escombe et al. [5] pointed out that the natural methods of encouraging airflow considerably prevent infections and respiratory diseases. However, in densely populated urban areas the natural ventilation efficiency is reduced due to interference among buildings. Thus, both effects of the arrangement and the spacing density of buildings in urban neighborhoods play an important role in providing optimal ventilation to ensure healthy and comfortable life conditions.

There are basically two types of natural ventilation, i.e. a) wind driven ventilation due to pressure differences in the atmosphere, b) stack ventilation due to temperature differences between indoor and outdoor areas. Teppner et al. [6] investigated air change rates by studying both ventilation mechanisms. Schulze and Eicker [7] reported that thermally and wind influenced natural ventilation can produce air change rates up to 5 h^{-1} in indoor spaces with a single opening. In the present study, the thermally induced airflow was out of the scope and only the wind driven ventilation was studied. The existing literature reports on various studies that focus solely on wind-induced airflows around and inside the buildings. Ernest et al. [8] evaluated natural ventilation performance of low-rise buildings based on the pressure distributions on the facades. Teppner et al. [6] reported that the wind-driven natural ventilation could be markedly improved in case of a suitable building orientation with respect to the prevailing wind. The influence of window type and opening area on ventilation was investigated by Heiselberg et al. [9].

Even though most of the studies on natural ventilation are focused on isolated buildings only, the effects of building interference on natural ventilation were recognized as well. Lee et al. [10] conducted wind-tunnel experiments to examine the wind load on a low-rise structure within an array of buildings of different spacing densities. Cheung and Liu [11] studied the sensitivity of the ventilation rate to building separation and disposition. It was found that the cross-ventilation rates were considerably larger with less densely spaced buildings.

The methods for studying natural ventilation include full-scale measurements, wind-tunnel experiments, and Computational Fluid Dynamics (CFD) simulations. In this study, the influence of buildings' spacing density on the ACH was studied in the atmospheric boundary layer wind tunnel. The scope was to determine the effects of various distances between buildings and different flow directions on ventilation rates in the studied cubic building model. The Air Change Rate (ACH) was initially determined for a stand-alone cubic building model

with two window openings. In subsequent experiments, an urban neighborhood in the 3 x 3 checkered square pattern was modeled using eight dummy objects placed around the main cubic building model. The air change was measured for different spacing densities between the cubic building models. In both cases, the experiments were conducted for various flow incidence angles and velocities. Both cross ventilation (both windows open) and single-side ventilation (only one window open) were investigated.

Some new aspects of the natural ventilation are provided with particular emphasis on the atmospheric boundary layer (ABL) characteristics and the Air Change Rate (ACH) estimation. The experimental setup includes wind-tunnel design, experimental technique and methodology. The obtained experimental results are presented and compared with previous studies and international standards and codes.

2   Characteristics of the atmospheric wind and natural ventilation

2.1   Atmospheric flow

Short-wave radiation from the sun is the basic mechanism that enhances atmospheric motions. Since Earth surface is heated unequally, pressure differences occur between different locations, which consequently causes airflows in the atmosphere.

Large-scale pressure differences determine local weather systems or even large planetary waves which may circumvent the entire globe and have a lifetime of several days. Small-scale pressure differences cause winds of limited duration, while smallest atmospheric motions represent turbulence which consists of small vortices of air with a characteristic lifetime of some minutes. Figure 2.1 shows an entire range of these phenomena presented as microscale, convective scale and macroscale, respectively [12]. Atmospheric motions usually take place in such a way that different patterns of motion are mutually independent both in time and space.
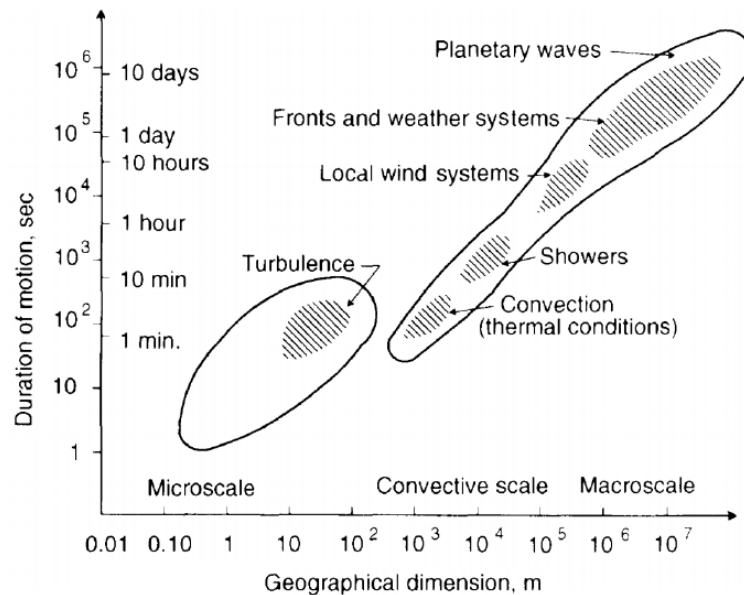
Figure 2.1: Patterns of motion in the atmosphere [12]

The motions of the air mass are predominantely in the horizontal and vertical directions. The horizontal motion of air is determined by the horizontal pressure forces, Coriolis force and the friction between the air and the underlying surface. The horizontal pressure gradient yields air movement from high to low pressure. If a parcel of air is observed on a line of constant pressure, called isobar, the force is perpendicular to an isobar. The pressure gradient is described as:

$$P = \frac{1}{\rho}\frac{\mathrm{d}p}{\mathrm{d}n}.$$

(2.1)

The Coriolis force is due to Earth rotation. The total motion of air has two components, i.e. the motion relative to the Earth as if the planet were fixed, and the motion given to the air mass by the Earth's rotation. When the atmosphere is viewed from a fixed point in space, Earth rotation is apparent and observer in space witnesses the total motion of the atmosphere. On the other hand, an observer on the ground sees and measures only the relative motion of the atmosphere, because he is also rotating and cannot see directly the rotational motion applied by the Earth. Instead, the observer on the ground sees the effect of the rotation as a deviation applied to the relative motion. The quantity that describes this deviation is the Coriolis force:

$$F_c = mfv, \tag{2.2}$$

where m is mass of air and v is velocity. Coriolis parameter f is defined as:

$$f = 2\omega \sin \phi, \tag{2.3}$$

where $\omega = 0.7272 \cdot 10^{-4}$ is the angular velocity vector of the Earth and ϕ is the angle of latitude. Wind velocity is decreased by the friction force, which weakens as the height above the surface increases. At a certain height, called gradient height δ, the friction force becomes negligible. This frictional influence from the Earth's surface forms the atmospheric boundary layer. Its typical velocity profile is shown in Figure 2.2.
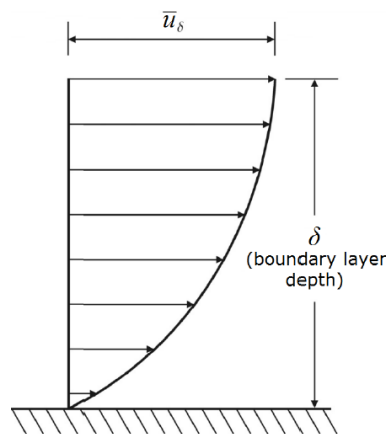
Figure 2.2: Velocity profile in the atmospheric boundary layer [3].

The pressure gradient force, Coriolis force and friction force generate equilibrium, illustrated in Figure 2.3.
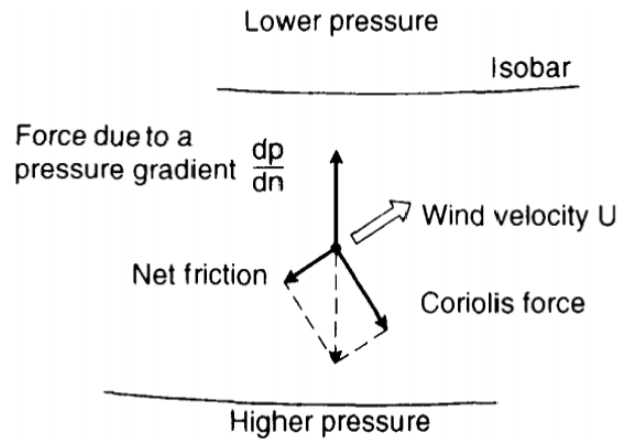
Figure 2.3: Equilibrium of forces in the atmosphere [12].

Since friction force decreases at higher altitudes above the surface, air velocity and consequently the Coriolis force increase. The equilibrium of forces yields a maximum deflection angle between isobars and direction of motion at the ground. The angle decreases to zero value when approaching the gradient height. Therefore, the wind in the atmospheric boundary layer is represented by twisted velocity profile known as the Ekman spiral, Figure 2.4, [12].
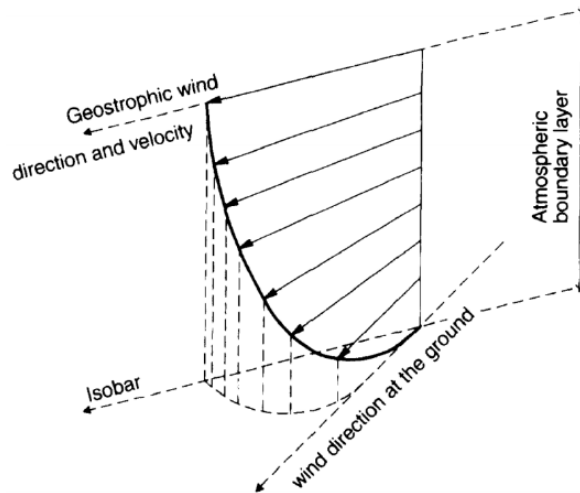
Figure 2.4: Schematic view of the Ekman spiral [12].

Besides horizontal forces, the motion of an elementary air mass is also determined by the vertical buoyancy force. It occurs when there is a temperature gradient between the air mass and the ambient air. The buoyancy force acts upwards, downwards or is equal to zero, which correspond to the unstable, stable, or neutral atmospheric stratification, Figure 2.5, [13].
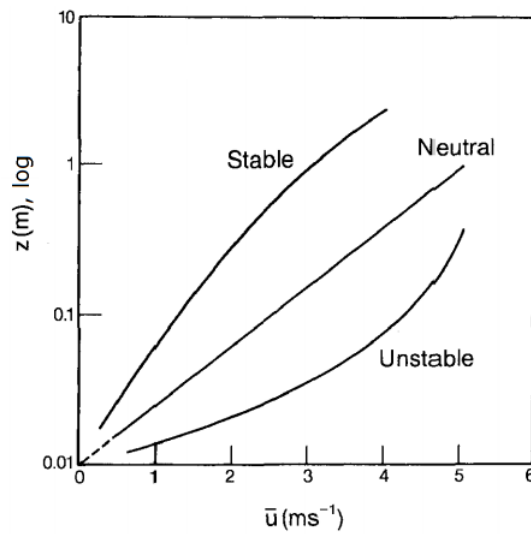
Figure 2.5: Wind profile in the stable, neutral, and unstable atmosphere, [13].

The logarithmic wind profile can be observed and it is valid for the neutrally stratified atmosphere. As the atmosphere becomes more stable or unstable, the profile starts to differ from the logarithmic profile.

2.2 Atmospheric boundary layer

The atmospheric boundary layer is defined as the part of the troposphere that is directly influenced by the presence of the Earth surface. It responds to surface forcing with a time scale of about an hour or less. As shown on Figure 2.6, it can be divided into two separate regions: inner and outer layer.
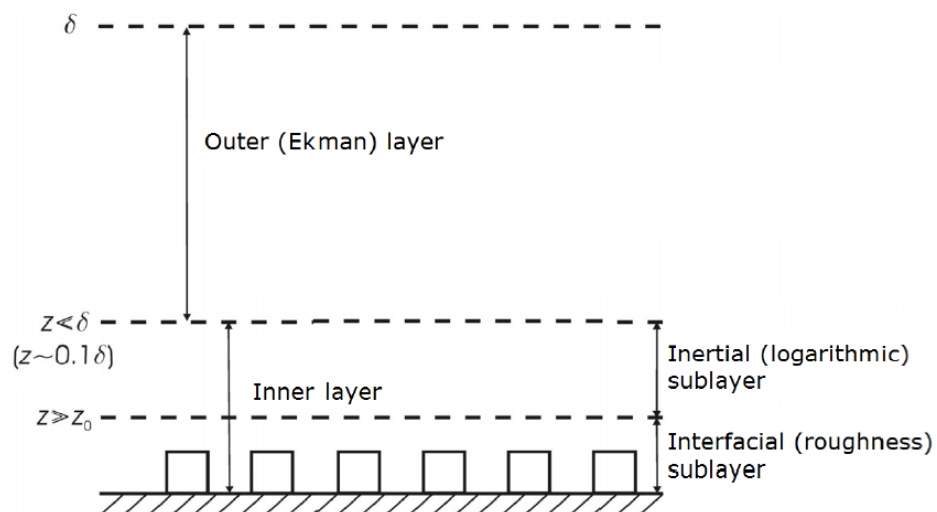
Figure 2.6: Structure of the atmospheric boundary layer, [3].

The mean properties of the flow (velocity, humidity and temperature) exhibit largest gradients in the inner region which extends throughout the lower $10 - 15\%$ of the ABL. This surface layer consists of the interfacial and inertial sublayers. The sublayer closest to the ground is the interfacial sublayer where the roughness of the underlying terrain plays a key role for the wind characteristics. Above the interfacial sublayer there is the inertial sublayer, where the dominant mechanisms of energy, mass and momentum transfer are turbulent stresses, while molecular diffusion can be neglected.

The outer layer, known as the Ekman layer, is the largest part of the ABL which extends up to 600 m [2]. In this height range, the flow shows negligible dependence on the terrain roughness and it is more influenced by the Coriolis force. The turbulent fluxes decrease with increasing height and they vanish in the upper Ekman layer. The area above the outer layer is the free atmosphere.

2.3   Mean velocity characteristics

Wind motions in the ABL are always turbulent. In order to describe the turbulent flow, the Reynolds decomposition of the total velocity is made into the mean velocity and the fluctuating velocity components in the longitudinal (x), lateral (y) and vertical (z) directions:

$$u(t) = \bar{u} + u'(t), \quad v(t) = \bar{v} + v'(t), \quad w(t) = \bar{w} + w'(t) \tag{2.4}$$

where the mean velocity is represented by an overbar and the fluctuating velocity by a prime. The mean velocity is calculated using the averaging procedure,

$$\bar{u} = \frac{1}{T} \int_{-T/2}^{T/2} u(t) \mathrm{d}t \tag{2.5}$$

Figure 2.7 shows the velocity profile in the ABL, where solid and dashed lines illustrate the instantaneous wind velocity and the mean velocity, respectively.
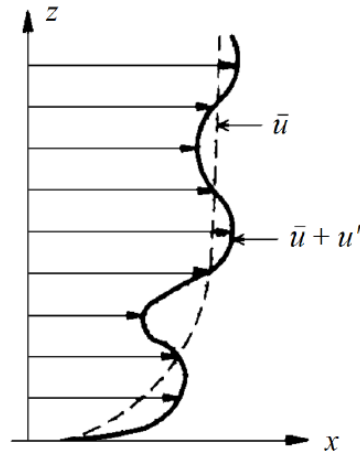
Figure 2.7: Velocity profile in the atmospheric boundary layer, [3].

Flow in the ABL is three dimensional; however, $\bar{v}$ and $\bar{w}$ components are commonly neglected because longitudinal velocity $\bar{u}$ is much larger compared to the $\bar{v}$ and $\bar{w}$ components. The vertical distribution of the mean longitudinal velocity is commonly defined using the power law:

$$\frac{\bar{u}_z}{\bar{u}_{ref}} = \left(\frac{z-d}{z_{ref}-d} \right)^{\alpha} = \left(\frac{\tilde{z}}{\tilde{z}_{ref}} \right)^{\alpha}, \tag{2.6}$$

where $\bar{u}_z$ is the mean velocity at height z, $\bar{u}_{ref}$ is the reference velocity at the reference height z_{ref}, d is displacement height and α is the exponent of the power law. The displacement height d is introduced when complex airflows near the ground in between the densely spaced obstacles (buildings, trees) are moved vertically out from the surface. In this case, the power law is valid above that displacement height, which is commonly between 75% and 100% of the height of the surrounding buildings. The exponent α depends on terrain roughness that is described by the aerodynamic surface roughness length z_0, Figure 2.8.
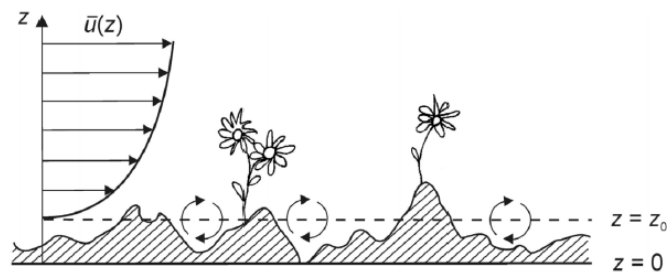
Figure 2.8: Simplified illustration of the aerodynamic surface roughness length z_0, [12].

z_0 depends on the height, shape, spacing density and arrangement of surface roughness elements. Table 2.1, [14] shows a classification of the terrain roughness, whereas different ABL velocity profiles for various surface roughness are illustrated in Figure 2.9.

Table 2.1: Classification of the effective terrain roughness according to Wieringa et. al, [14].

Class	z_0 (m)	Landscape description
1. Sea	0.00002	Open sea or lake , tidal flat, snow-covered flat plain, featureless desert, tarmac and concrete with a free fetch of several kilometres.
2. Smooth	0.005	Featureless land surface without any noticeable obstacles and with negligible vegetation; e.g. beaches, pack ice without large ridges, marsh or open country.
3. Open	0.03	Level country with low vegetation (e.g. grass) and isolated obstacles with separations of at least 50 obstacle heights; grazing land without wind breaks, heather, moor and tundra, runway area of airports. Ice with ridges across-wind.
4. Roughly open	0.1	Cultivated or natural area with low crops or plant covers, or moderately open country with occasional obstacles (e.g. low hedges, isolated low buildings or trees) at relative horizontal distances of at least 20 obstacle heights.
5. Rough	0.25	Cultivated or natural area with high crops or crops of varying height, and scattered obstacles at relative distances of 12–15 obstacle heights for porous objects (e.g. shelterbelts) or 8–12 obstacle heights for low solid objects (e.g. buildings).
6. Very rough	0.5	Intensively cultivated landscape with many rather large obstacle groups (large farms, clumps of forest) separated by open spaces of about eight obstacle heights. Low densely planted major vegetation like bush land, orchards, forest. Also, area moderately covered by low buildings with interspaces of three to seven building heights.
7. Skimming	1.0	Landscape regularly covered with similar-size large obstacles, with open spaces of the same order of magnitude as obstacle heights; e.g. mature regular forests, densely built-up area without much building height variation.
8. Chaotic	$2.0 < 8.0$	City centres with mixture of low-rise and high-rise buildings, or large forests of irregular height with many clearings.
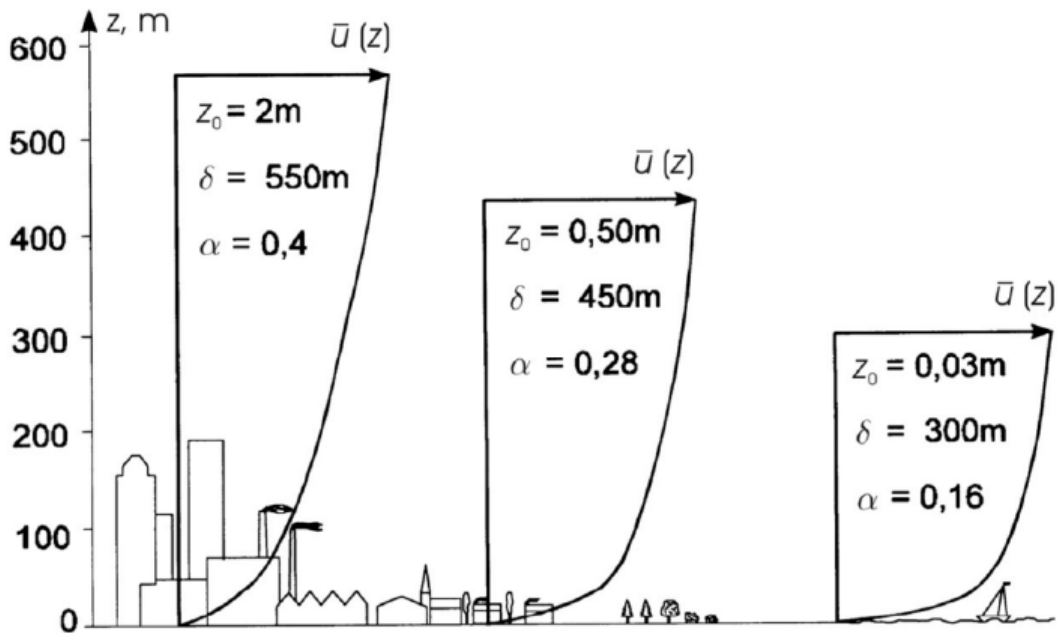
Figure 2.9: Velocity profiles in the atmospheric boundary layer for various surface roughness, [15]

In the lower 10% of the ABL (surface layer), the logarithmic law can be used as well,

$$\frac{\overline{u}_z}{u_\tau} = \frac{1}{\kappa} \ln \frac{z-d}{z_0}, \tag{2.7}$$

where u_τ is friction velocity and κ is von Kármán constant with the standard value of $\kappa = 0.4$.

2.4 Turbulence characteristics

Turbulence is a flow regime characterized by chaotic changes in pressure and flow velocity, which is caused by dissipation of the wind kinetic energy into thermal energy via creation and progressive destruction of smaller eddies (energy cascade). The airflow within the ABL is highly turbulent and it considerably affects objects situated on the ground surface. Due to the wind turbulence, engineering structures are subject to unsteady loads, so the structural vibrations are enhanced that can cause severe damage. It is thus necessary to get to know atmospheric turbulence in great detail. The relevant characteristic parameters of the atmospheric turbulence are turbulence intensity, integral length scale of turbulence, Reynolds stress and power spectral density of velocity fluctuations.

2.4.1 Turbulence intensity

Turbulence intensity in the longitudinal (x) direction is defined as:

$$I_u(z) = \frac{\sqrt{\overline{u'^2}(z)}}{\overline{u}_{ref}}, \qquad (2.8)$$

where $u'(z)$ is the fluctuation of the mean velocity $\overline{u}$ at height z, $\overline{u}_{ref}$ is reference mean velocity. $\overline{u}_{ref}$ is commonly determined at the gradient height δ, in the measuring point height or at the height of the top surface of the studied structural model. The longitudinal turbulence intensity is larger than lateral and vertical intensities that are defined as:

$$I_v(z) = \frac{\sqrt{\overline{v'^2}(z)}}{\overline{v}_{ref}}, \quad I_w(z) = \frac{\sqrt{\overline{w'^2}(z)}}{\overline{w}_{ref}}. \qquad (2.9)$$

The ratio of the RMS values of fluctuations is constant near the ground [2]:

$$\frac{\sqrt{\overline{v'^2}(z)}}{\sqrt{\overline{u'^2}(z)}} = 0.75, \quad \frac{\sqrt{\overline{w'^2}(z)}}{\sqrt{\overline{u'^2}(z)}} = 0.5. \qquad (2.10)$$

The turbulence intensity is maximal close to the ground and it decreases with increasing the height from the surface.

2.4.2 Integral turbulence length scales

Turbulent flow is considered as a sum of vortices carried by a mean velocity in the main flow direction. Each eddy is characterized by a periodic motion of circular frequency $\omega = 2\pi f$, where f is frequency. Quantities describing the average size of the energy-containing eddies in a turbulent flow are integral turbulence length scales. There are in total nine integral turbulence length scales (three dimensions combined with three velocity directions).

The most relevant integral length scale is L_u^x, which describes average size of eddies in the longitudinal direction caused by velocity pulsations in the longitudinal direction:

$$L_u^x = \int_0^\infty R_u^x(\Delta x) \mathrm{d}\Delta x, \qquad (2.11)$$

where the correlation factor R_u^x is defined as:

$$R_u^x(\Delta x) = \frac{\overline{u_1'(t) \cdot u_2'(t)}}{\sqrt{u_1'^2} \cdot \sqrt{u_2'^2}} \qquad (2.12)$$

Indices 1 and 2 indicate two different points in space. R_u^x is commonly calculated by assuming the Taylor's frozen turbulence hypothesis, which indicates that velocity fluctuations are moving with the mean flow velocity in the main flow direction:

$$R_u^x(\Delta x) = \frac{\overline{u_1'(t) \cdot u_1'(t - \Delta t)}}{\overline{u_1'}^2} = R_u^x(\Delta t); \quad \Delta t = \frac{\Delta x}{\overline{u}}. \tag{2.13}$$

Integral turbulence length scale is then calculated as:

$$L_u^x = \overline{u} \int_0^\infty R_u^x(\Delta t) \mathrm{d}\Delta t. \tag{2.14}$$

2.4.3   Reynolds shear stress

Friction forces predominantly occur at the contact point of the air flow and the ground. They are transmitted in the upper parts of the atmosphere through shear stress, which is equal to the sum of the viscous and turbulent (Reynolds) stress:

$$\tau = \mu \frac{\partial \overline{u}}{\partial z} - \rho \overline{u'w'}. \tag{2.15}$$

The viscous stress $\mu \frac{\partial \overline{u}}{\partial z}$ is at maximum on the surface and it decreases with increasing the height. The turbulent Reynolds shear stress $\rho \overline{u'w'}$ is equal to zero on the surface and it increases with increasing the distance from the ground. Within the inertial sublayer the Reynolds shear stress is approximately constant (Prandtl constant-flux layer). In the outer layer of the ABL, Reynolds shear stress starts reducing as the height increases until it is equal to zero at the upper edge of the ABL. In wind engineering and environmental aerodynamics, only $\overline{u'w'}$ component of the Reynolds shear stress in anisotropic flows is commonly considered, while components $\overline{v'w'}$ and $\overline{u'v'}$ are neglected.

2.4.4   Power spectral density of longitudinal velocity fluctuations

Power spectral density function, usually called power spectrum, presents velocity fluctuations as a function of frequency. Distribution of the turbulence kinetic energy over frequencies is described by the turbulence kinetic energy spectrum. In the longitudinal direction it is defined as:

$$\sigma_u^2 = \int_0^\infty S_u(f) \mathrm{d}f, \tag{2.16}$$

where σ_u is standard deviation of absolute velocity in the longitudinal direction u, $S_u(f)$ is the amplitude (or power) of longitudinal velocity fluctuations at the frequency f.

In airflows developing above rough surface large eddies progressively dissipate into smaller ones. Furthermore, during dissipation, the kinetic energy is transferred from larger to smaller eddies, thus producing a hierarchy of eddies. This process is called energy cascade. The largest eddies (at low frequencies) are the energy-containing eddies. The eddies somewhat smaller than the largest eddies carry the most of the energy. In the inertial subrange, energy is transferred to smaller eddies. This range is in accordance with the Kolmogorov model:

$$ S_u(f) \approx k_w^{-2/3}, \tag{2.17} $$

where k_w is the wave number of the eddies. In the high frequency dissipation range, molecular diffusion dominates and the kinetic energy is converted into internal (thermal) energy. Schematic representation of the velocity power spectrum and an example of the power spectrum by Kozmar, [16] are given in Figure 2.10 and Figure 2.11, respectively.
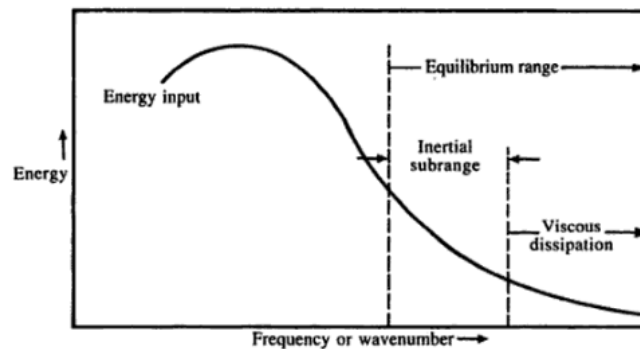
Figure 2.10: Schematic representation of the power spectrum of velocity fluctuations, [17]
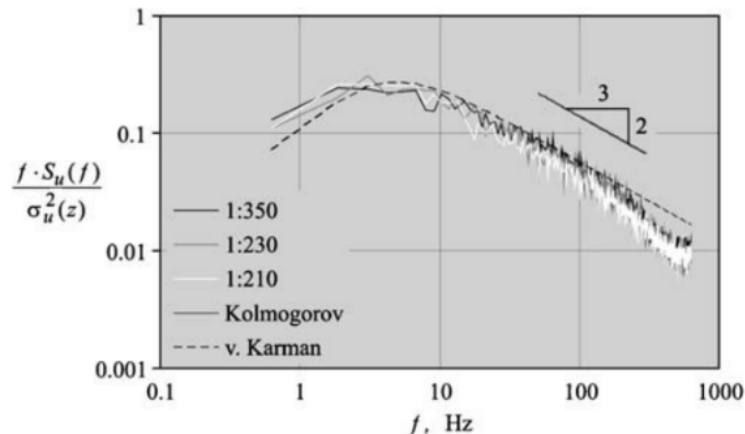
Figure 2.11: Example of power spectral density of longitudinal velocity fluctuations, [16].

The spectrum of the turbulence kinetic energy in the longitudinal direction with distinct macrometeorological and micrometeorological areas, two main peaks and a spectral gap between them are shown in Figure 2.12. In wind engineering and environmental aerodynamics, the focus is predominantely on the micrometeorological range.
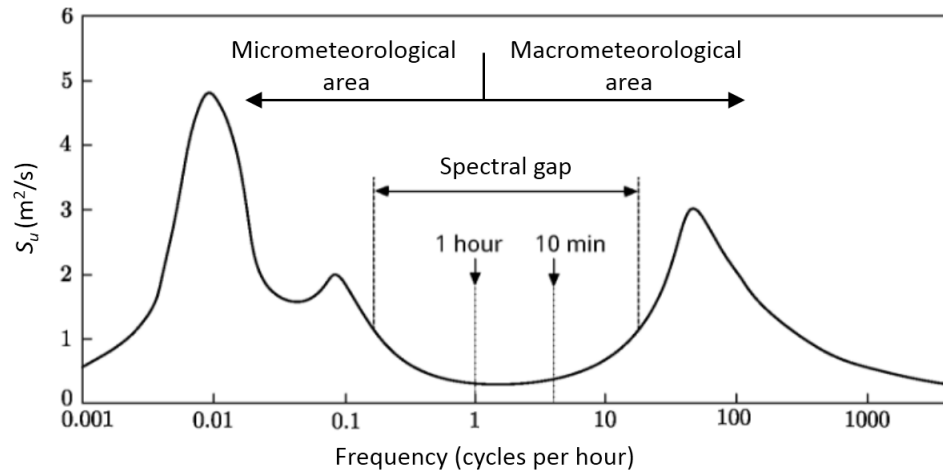
Figure 2.12: Spectrum of the turbulence kinetic energy in the atmosphere proposed by van der Hoven, [18]

2.5   Flow around the cube

Engineering structures influenced by the wind flow can be prone to vibration (e.g. long bridges and tall slender buildings) and bluff structures that do not vibrate (e.g. low-rise buildings). For purposes of this study, the cubic buildings are considered not to be prone to vibration and treated that way.

Forces acting on objects are proportional to the square of velocity:

$$F = \frac{1}{2}\rho u^2 A c_F \tag{2.18}$$

where ρ is air density, u is wind velocity, A is surface area and c_F is dimensionless force coefficient. Figure 2.13 shows characteristic pressure distribution on a cubic building subjected to the wind.
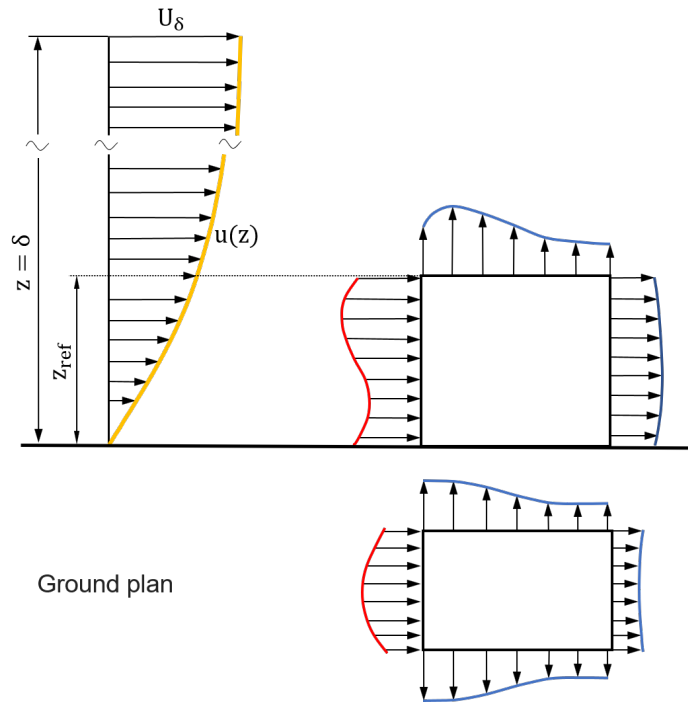
Figure 2.13: Pressure distribution on a cube, [19]

Pressure is positive only on the front surface where the wind kinetic energy is converted into pressure. The pressure is at maximum at about 70% of the building height (stagnation zone). Flow separation, which is characteristic for objects with sharp edges (bluff bodies), occurs on the top and side surfaces, leading to negative surface pressure in those areas. After separation, flow sometimes reattaches on these sides, i.e. for larger incoming turbulence the reattachment occurs closer to the leading edge. A schematic view of the complex flow around a cube is given in Figure 2.14, [20].
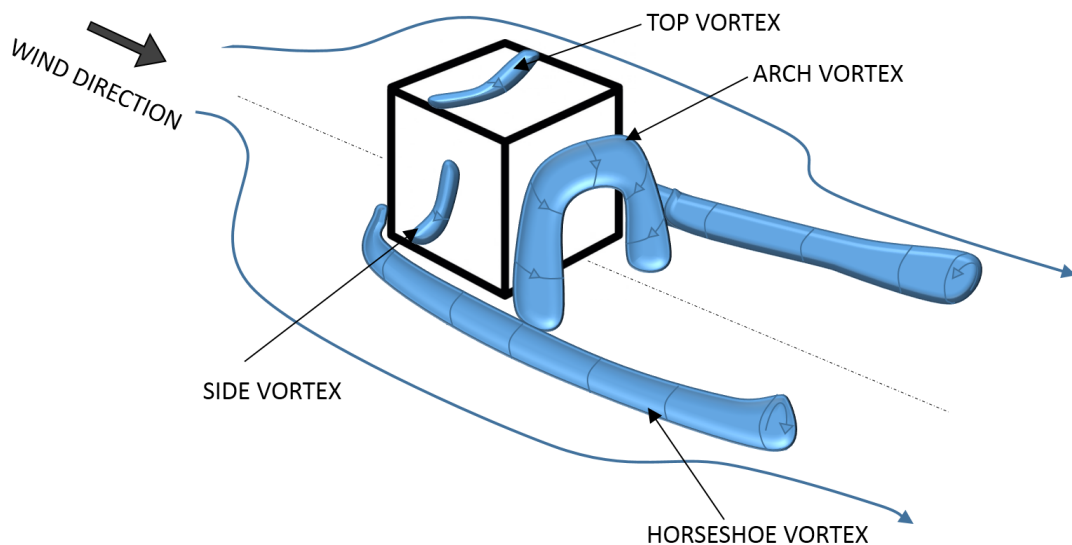
Figure 2.14: Schematic view of the flow around a cube, adapted from Martinuzzi and Tropea [20]

Due to a complex flow structure around a cube, a turbulent horseshoe vortex develops upstream of the cube, [21], [22]. Corner and top surface vortices are generated along the sides and top surfaces of the cube, and there is an arch vortex generated in the wake of the cube.

2.6 Natural ventilation

Natural ventilation refers to the flow of external air to an indoor space through various openings on the building, as a result of pressure differences due to natural forces. Nowadays, most of the buildings are still ventilated through doors or windows. The exchanged volume of air divided by the total indoor volume to be ventilated is the air change rate (ACH). The result of the ACH is the number of times the air within a defined space is replaced per unit of time, usually one hour. According to [23], ACH is defined as:

$$\text{ACH} = \frac{\dot{V}}{V_R},\tag{2.19}$$

where V_R is total volume of the indoor space, $\dot{V}$ is volume flow rate defined using the orifice equation:

$$\dot{V} = C_D A \sqrt{\frac{2\Delta p}{\rho}}.\tag{2.20}$$

Term $\sqrt{2\Delta p/\rho}$ represents velocity derived from pressure difference and air density ratio, A is cross sectional area, C_D is nondimensional discharge coefficient defined as the ratio between the actual flow discharge and the theoretical flow discharge at the building opening. The largest value of the discharge coefficient C_D is obtained for flows perpendicular to fully open windows, while it is smaller for oblique winds and partially blocked openings. For wind not perpendicular to the openings (i.e. incidence angle $\beta \neq 0°$), a new projected cross sectional area A' has to be taken into account when calculating ACH. Volume flow rate $\dot{V}$ can also be calculated as:

$$\dot{V} = C_v A U_\infty,\tag{2.21}$$

where U_∞ is wind velocity and C_v is effectiveness of the openings with assumed values of $C_v \approx 0.6$ for flows perpendicular to the building facade.
Wind-driven ventilation depends on wind direction and velocity, pressure distribution, arrangement and spacing density of openings on the facade of the building and the ventilating behavior of the user. Thus, finding accurate estimation of ventilation is a complex and difficult

task. Wind-driven natural ventilation can be classified as cross ventilation and single-side ventilation. In the present work, both cases were studied.

3   Experimental setup

3.1   The IFMHT-GUT boundary layer wind tunnel

The wind tunnel experiments were carried out in the boundary layer wind tunnel of the Institute of Fluid Mechanics and Heat Transfer at the Graz University of Technology, Austria. It is a Göttingen closed-circuit type of a wind tunnel that is designed to simulate the atmospheric boundary layer as well as for various applications in wind engineering and environmental aerodynamics, Figure 3.1.

Figure 3.1: IFMHT-GUT boundary layer wind tunnel, [23].

It has an 8.6 m long closed test section and an adjustable ceiling to allow for achieving nearly zero pressure gradient along the test section. The rectangular cross section is 2 m wide and 1 m high. At the end of the test section there is a turntable that allows simulation of wind effect on structures at various flow incidence angles. The flow velocity can be regulated up to a maximum value of 31 m/s.

In order to simulate the lower part of the ABL, a combination of a grid of rods at the nozzle exit, a tripping barrier wall in the form of a saw tooth tread design, and surface roughness elements are used. Between cylindrical rods of the grid, the spacing is unequal, which is shown in Figure 3.2, [23].
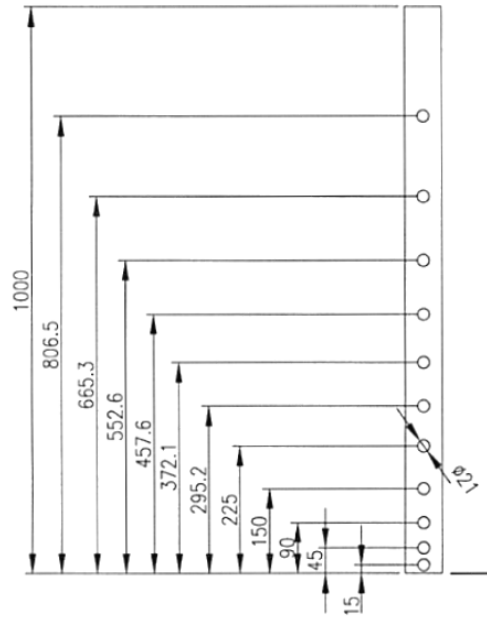
Figure 3.2: Design of a cylindrical rod grid, [23]

Basic Lego and Lego Duplo bricks were used as surface roughness elements. The test section area in front of a measuring position was covered with bricks as suggested by Langensteiner, Figure 3.3, [23].

Figure 3.3: Test section floor covered with surface roughness elements, [23]

The basal area index, which represents the ratio between the test section area covered with surface roughness elements and the total test section area in front of a measuring position, is 3.6%. The test section floor pattern consists of 19 equally aligned rows, each having 11 equally spaced Lego Duplo bricks. Between the second and the third row that are closest to the measuring position, another row of 10 basic Lego bricks is inserted. It should be noted, that

in the six rows closest to the measuring position, two connected Lego Duplo bricks were used instead of only one which is the case in all the remaining rows. Test section floor with detailed positioning of the roughness elements is given in Figure 3.4 and Figure 3.5.
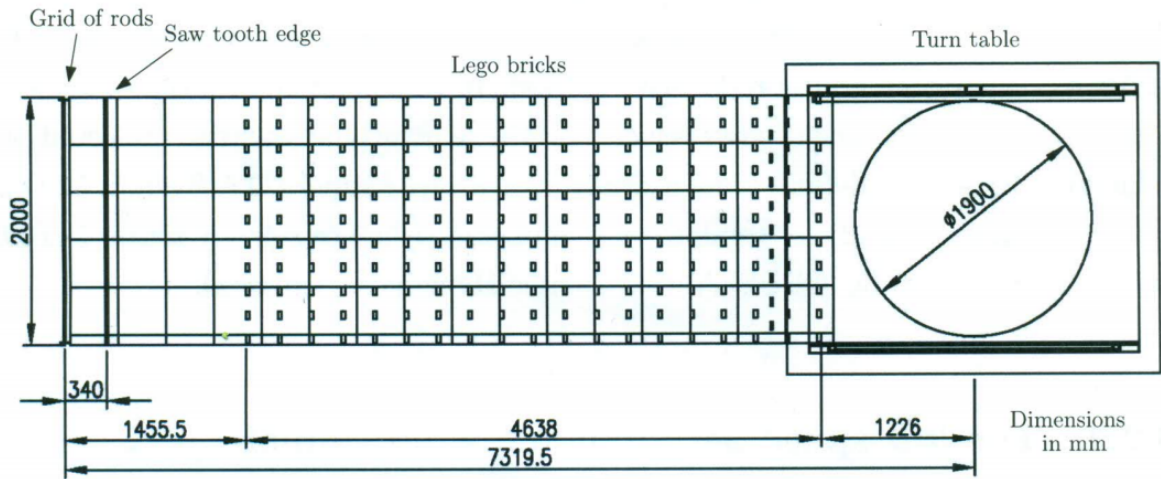

Figure 3.4: Arrangement of the grid rods, barrier wall, surface roughness elements in IFMHT-GUT wind tunnel with dimensions given in mm [23]
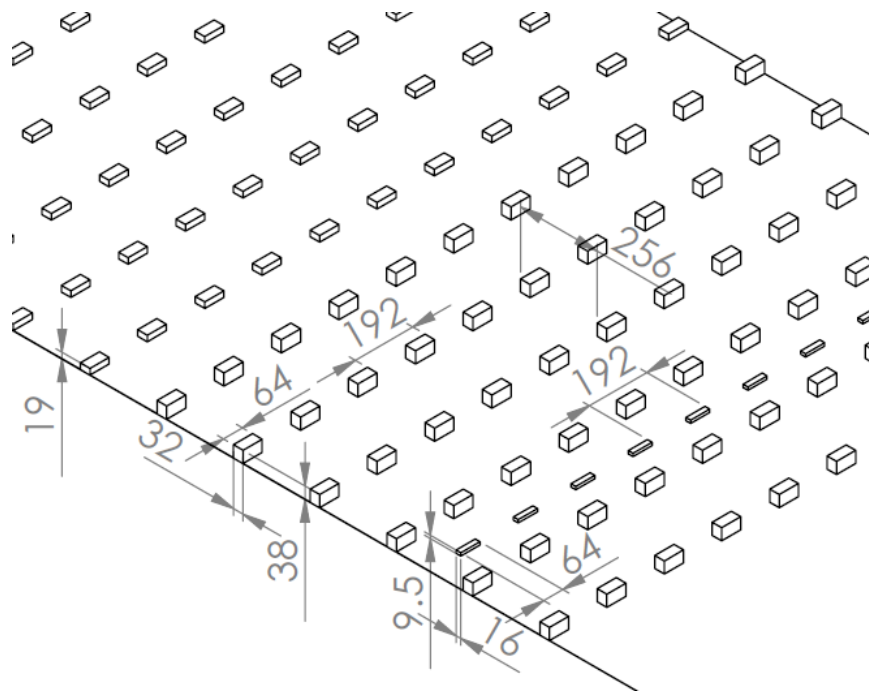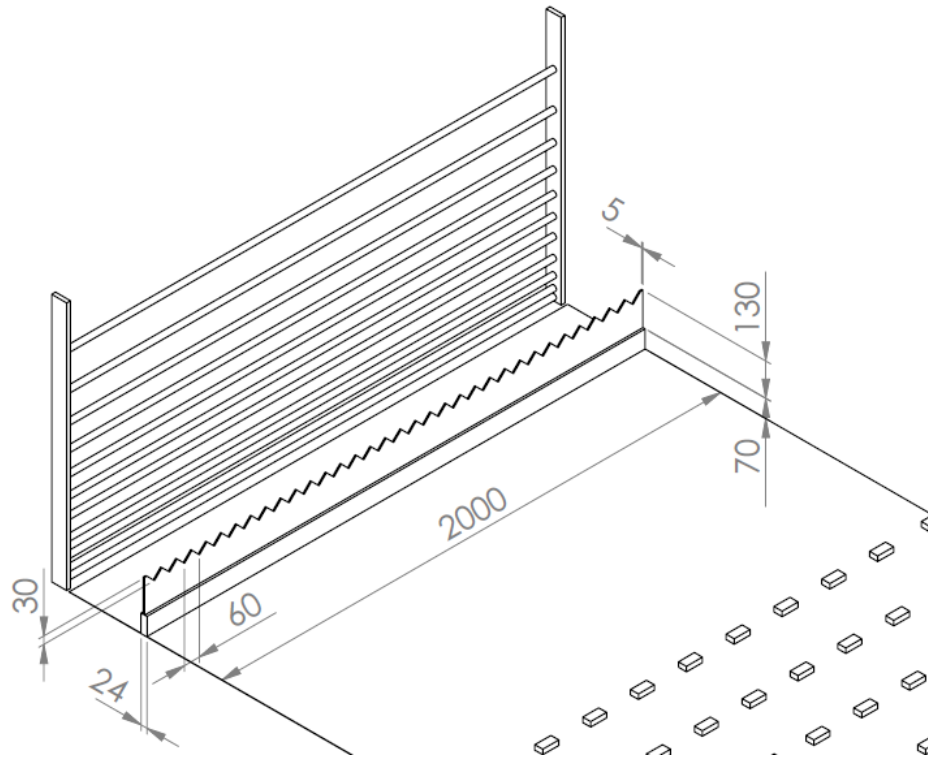

Figure 3.5: Arrangement of surface roughness elements with dimensions given in mm

Detail sketch and dimensions of the saw tooth edge is shown in Figure 3.6.

Figure 3.6: Dimensions and positioning of a barrier wall with dimensions given in mm

3.2 Hot-wire anemometry system

Hot-wire anemometry was used for velocity measurements. The method relies on the changes in heat transfer from a heated sensor exposed to the fluid flow. The sensor usually has the shape of a small cylindrical wire or a thin film, stretched between needle-shaped prongs. It is made out of material whose electric resistance is temperature dependent. Four types of sensors are available, i.e. miniature wires, gold-plated wires, fibre-film or film-sensors, Figure 3.7, [24].
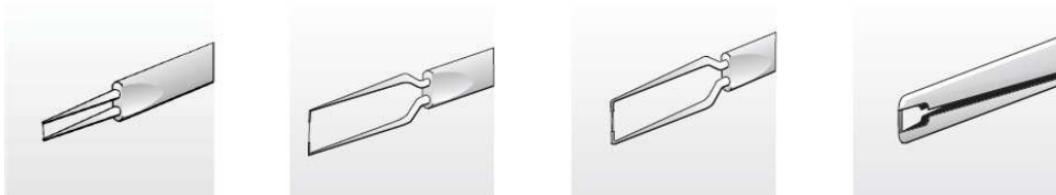
Figure 3.7: Miniature wires, gold-plated wires, fibre-film and film-sensors, [24].

Wires are normally 5 μm in diameter and 1.2 mm long. Gold-plated wires have the same active length but are copper- and gold-plated at the ends to a total length of 3 mm in order to minimize prong interference. Fibre-sensors are quartz-fibers, commonly 70 μm in diameter and with 1.2 mm active length, covered by a nickel thin-film, which is protected by a quartz coating. Fibre-sensors are mounted on prongs in the same arrays as wires. Film sensors consist of nickel thin-films deposited on the tip of aerodynamically shaped bodies, wedges or cones,

[24].

Anemometer probes are commonly available in one-, two- and three-dimensional versions as single-, dual- and triple-sensor probes, respectively, where each sensor measures one velocity component, Figure 3.8, [24].
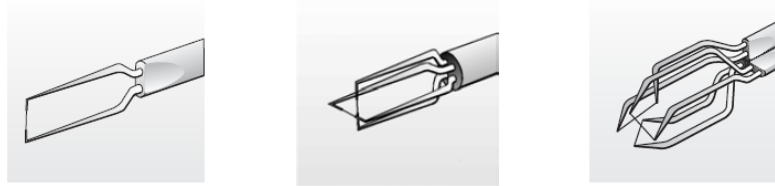
Figure 3.8: One-, two- and three-dimensional hot-wire sensors, [24]

In this study, Dantec Dynamics 55P61 dual-sensor X wire probe was used for measurements, Figure 3.9, [25]. It can simultaneously measure two velocity components and should be mounted with the probe axis parallel to the main flow direction, so that the predominant flow vector impinges the two wires at an incidence angle of $45°$.

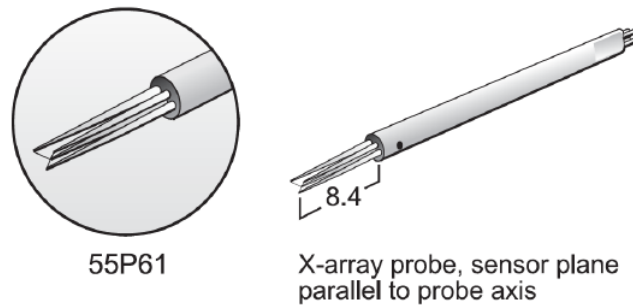**Figure 3.9: Dantec dynamics X wire probe, [25].**

Hot-wire anemometry operating principle is based on cooling of the preheated wire exposed to the fluid flow. An electric current is emitted through the sensor, thus causing the wire to heat. As the fluid flows over the device, it cools the sensor, removing some of its heat energy. The basic heat balance for steady flow between the heating and the cooling is:

$$R_w I_w^2 = (T_w - T_a)\phi_{conv}(U).$$ (3.1)

Since the heat convection function $\phi_{conv}(U)$ primarily depends on a fluid velocity normal to the sensor, the flow velocity can be determined from the current intensity I_w, heated sensor resistance R_w, heated wire temperature T_w and unheated wire temperature T_a. For unsteady turbulent flow, heat balance is expressed as:

$$m_w c_w = R_w I_w^2 - (T_w - T_a)\phi_{conv}(U), \tag{3.2}$$

where the left-hand side represents thermal energy stored in the sensor, m_w is mass of the sensor, c_w is specific heat of the sensor material.

Hot-wire anemometry devices can be classified as CCA (Constant Current Anemometer), CVA (Constant Voltage Anemometer) and CTA (Constant Temperature Anemometer). In the CCA operating mode, the electric current I_w is constant and the change in resistance R_w due to the flow velocity is measured. In the CVA systems, $R_w I_w$ representing voltage is constant and the change of the current I_w is measured. The CTA systems maintain the sensor temperature and thus the resistance R_w constant. The change in the electric current I_w due to changes in fluid velocity is measured.

In this study, a CTA hot-wire anemometer is employed using the Wheatstone bridge. An example of a CTA Wheatstone bridge circuit is shown in Figure 3.10.
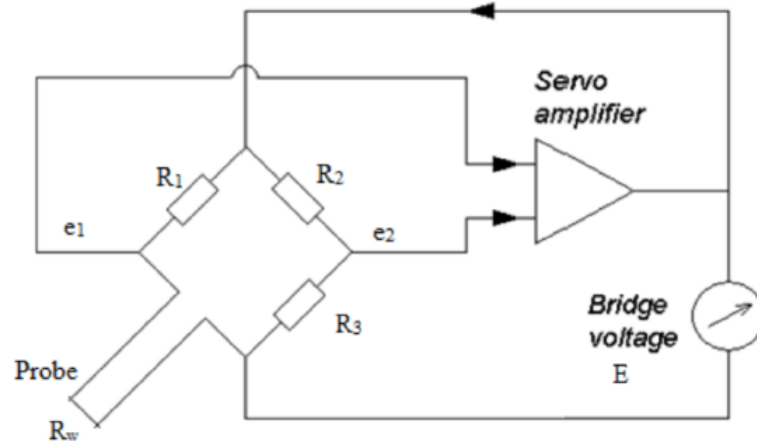

Figure 3.10: Schematic view of the Wheatstone bridge, [24].

The circuit is composed of two fixed resistors R_1 and R_2 and the third variable resistor R_3. The hot-wire probe acts as the fourth resistor R_w that completes the bridge. The bridge is balanced when $R_1/R_w = R_2/R_3$, resulting in zero voltage difference between points 1 and 2.

The constant temperature circuit makes advantage of the fact that the wire resistance R_w is temperature dependent. When the wire temperature and resistance are at some initial operating point, the variable resistor R_3 can be adjusted to balance the bridge. As the air velocity varies, the temperature of the wire and consequently resistance changes. This effect causes the bridge to become unbalanced, resulting in a voltage difference between points 1 and 2. The amplifier senses that difference and accordingly adjusts the feedback to keep the wire temperature and resistance constant, and thus re-balances the bridge. These changes in electric current can be measured and used to calculate the flow velocity over the wire.

In the present study, Dantec Dynamics multichannel CTA system 54N82 was used. It is used combined with other equipment, Figure 3.11, [24]. The measuring chain consists of a probe with probe support and cabling, CTA anemometer, signal conditioner, A/D converter, and PC equipped with the software.
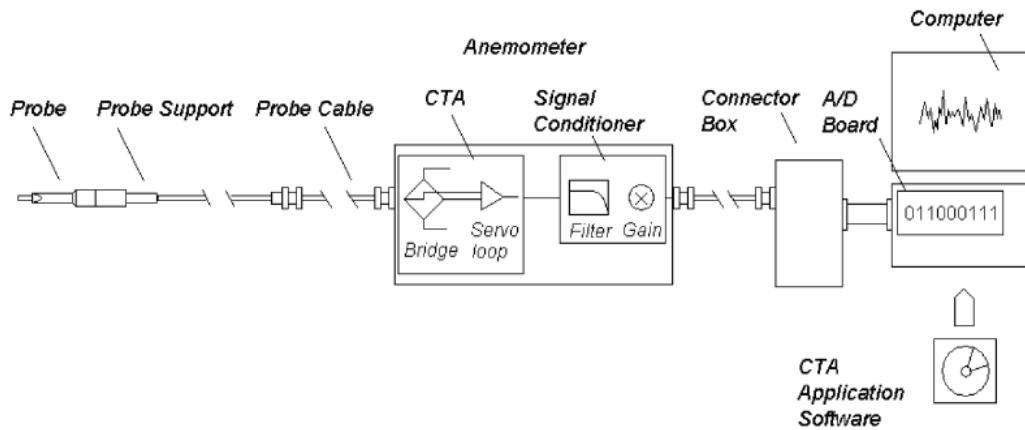

Figure 3.11: Typical Constant Temperature Anemometry (CTA) system, [24]

Since vertical velocity profiles are investigated a traverse system was installed for positioning the CTA probe. Its task is to automate the movement of a probe between the measurement points. The vertical motion is remotely controlled using Dantec Dynamics MiniCTA software. Positioning in lateral direction is done manually with the probe support in order to enable velocity profile estimation in various planes.

3.3 Tracer gas system

Tracer gas measurements were carried out to determine ACH. The infrared Multi Gas Monitor Innova 1316A-2 by LumaSense Technologies was used for monitoring concentration of a tracer gas inside the cubic building model. The concentration measurement principles are based on Non Dispersive Infrared Sensors (NDIR). The NDIR method uses fixed, non-scanning infrared light frequencies to characterize gas concentrations. The concentration of a gas volume is a function of the quantity of gas molecules in the sample. The absorption of infrared light increases with the number of gas molecules in the light path. With increase in concentration of infrared-absorbing gas, the transmission of infrared light decreases. A basic NDIR measurement system is shown in Figure 3.12.
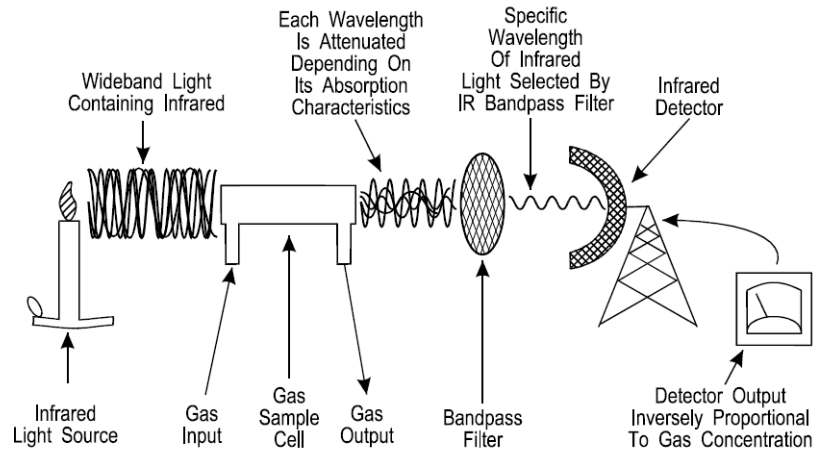
Figure 3.12: Schematic view of Non Dispersive Infrared (NDIR) system, [26].

The main elements of the NDIR system include infrared light source, sample cell, infrared filter and infrared detector. The source generates wide range of light at frequencies covering the infrared band. Light passes through the sample cell that contains the sample gas. The cell is made out of gold-coated glass with two infrared-transparent windows providing the passage of light through the chamber. An optical band pass filter is used to select a specific band of infrared light. The filter wavelength depends on the gas that is measured. The light not absorbed by the gas reaches a detector that produces output voltage proportional to the measured light.

The tracer gas used in this study was carbon dioxide CO_2. It is easy to analyze, chemically stable, inert and neither flammable nor explosive, thus meeting all the requirements for successful air change measurements in the present study.
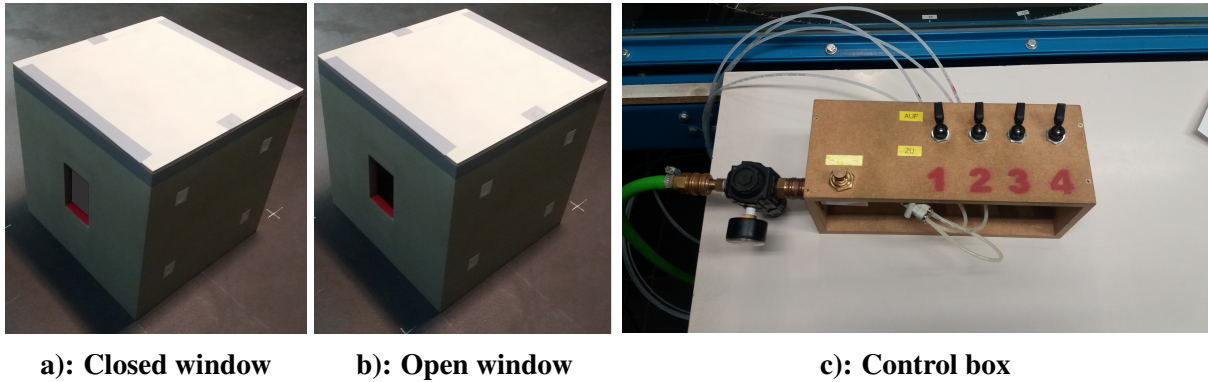
3.4   Cubic building model

In this work, natural ventilation was investigated for a cubic building model with two openings (windows) in opposing surfaces. The studied cubic building model and its dimensions are presented in Figure 3.13.
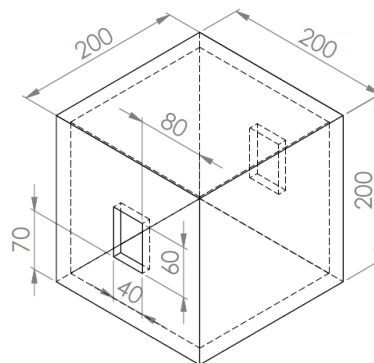
Figure 3.13: Schematic view of the studied building model with dimensions provided in mm

The inner surface of the walls was coated with a special enamel to suppress diffusion of tracer gas (CO_2) through the wooden material. The opening and closing of windows was achieved using pneumatically driven wooden sliders that were manually controlled using the switches on the control box, Figure 3.14.

a): Closed window   b): Open window   c): Control box

Figure 3.14: a) and b) Cubic building model with closed and open windows; c) Control box for controlling pneumatically driven sliders

For single-side ventilation measurements, an appropriate thin cover was made to permanently close and suppress leakage on one of the windows, Figure 3.15. Besides studied building model, another eight identical dummy models, which represent buildings in urban neighborhood, were manufactured. Their shape and dimensions match those from the main studied cubic building model (20x20x20 mm).

Figure 3.15: Cubic building model with a thin cover on the window

3.5   Methodology

3.5.1   Velocity measurements

The CTA system with the dual-sensor X wire probe was used for simultaneous velocity measurements in longitudinal and vertical directions. The probe was mounted on the traverse located at the cross plane at the beginning of the measuring section, Figure 3.16. For achieving a fine resolution, in total 48 measuring points in a vertical span of 713 mm were

used. Since velocity gradients are larger close to surfaces, the measuring points were more densely arranged at the locations near the test section floor. A Dantec Dynamics reference velocity sensor 54T29 used for measuring free stream reference velocity was set at the beginning of the test section at a height of 500 mm, Figure 3.17. This allows adjustment of the tunnel velocity without using the X-wire probes.


Figure 3.16: Hot-wire probe mounted on a traverse in the IFMHT-GUT wind tunnel

Figure 3.17: Reference velocity sensor 54T29 mounted on the IFMHT-GUT wind tunnel wall

The ABL simulations were carried out for four different velocities (3, 5, 7 and 10 m/s). To check uniformity of the flow in the lateral direction, the measurements with flow velocity $u = 5$ m/s were carried out in the middle plane and two planes 250 mm offset to left- and right-hand side, denoted as y_C, y_L and y_R, respectively, Figure 3.18.
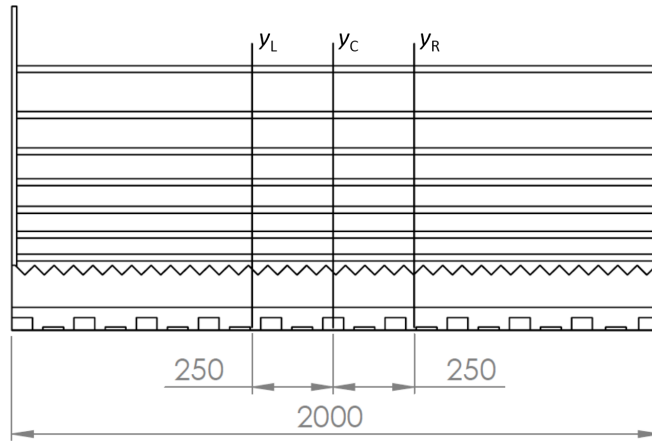
Figure 3.18: Positions of measuring planes in the lateral direction

The time record length for each measurement point was 50 s at the sampling rate of 10 KHz.

3.5.2 Tracer gas measurements

Ventilation flow rates were obtained using the concentration decay method. Initially, indoor space of the cubic building model was filled with tracer gas CO_2 with both windows closed. After air and CO_2 were homogeneously mixed, windows were open using switches on a control board for fixed time interval $\Delta t = t_2 - t_1$. During the time interval, the indoor mixture was interacting with the external flow field. According to Langensteiner [23], the conservation of the mass m of the tracer gas within a single zone in contact with the outdoor environment is:

$$\frac{\mathrm{d}m}{\mathrm{d}t} = C_o \dot{m}_{oi} - C_i \dot{m}_{io} + E, \tag{3.3}$$

where C is tracer gas mass concentration, $\dot{m}$ is mass flow rate and E is mass injection rate of the tracer gas. Indoor and outdoor environment is denoted by subscripts i and o, respectively. For instance, $\dot{m}_{io}$ indicates flow rate from indoor to outdoor space. The mass of tracer gas is related to the mass of air M by:

$$m = C_i M, \tag{3.4}$$

where C_i is concentration of the tracer gas in the indoor air. Assuming that the mass flow rates in and out of the studied indoor space are equal, $\dot{m}_{oi} = \dot{m}_{io} = \dot{m}$, Eq. (3.3) modifies to:

$$M \frac{\mathrm{d}C_i}{\mathrm{d}t} = \dot{m}(C_i - C_o) + E. \tag{3.5}$$

Since there is no gas injection during the measurement process when the windows are open and the interaction between the internal and the external air is enabled, E can be neglected. Additionally, with $\Delta C = C_i - C_o$, the mass flow rate is:

$$\dot{m} = \frac{M\dfrac{\mathrm{d}C_i}{\mathrm{d}t}}{\Delta C}. \tag{3.6}$$

By integrating Eq. (3.6) over a given period of time and introducing $M = \rho V_R$ and $\dot{m} = \rho \dot{V}$, where ρ is the constant air density, V_R is the volume of observed space and $\dot{V}$ is volume flow rate, ACH is calculated as:

$$\text{ACH} = \frac{\dot{V}}{V_R} = \frac{1}{\Delta t} \ln \frac{\Delta C(t)}{\Delta C(t + \Delta t)}. \tag{3.7}$$

Using LumaSense BZ6013 – 1316A-2 software connected to the tracer gas system, CO_2 concentration was measured at two times t_1 and t_2, i.e. right before the opening and right after closing the windows. The process was repeated for several times for each configuration in order to obtain average ACH values. These values were then scaled using the calculated scaling factor. For the same velocity u, the ACH in model scale is given as:

$$\text{ACH}_m = \frac{\dot{V}_m}{V_{R,m}} = \frac{u A_m}{V_{R,m}}, \tag{3.8}$$

while ACH in the real scale is:

$$\text{ACH}_r = \frac{\dot{V}_r}{V_{R,r}} = \frac{u A_r}{V_{R,r}}, \tag{3.9}$$

A scale of $1 : m$ then yields:

$$\frac{\text{ACH}_r}{\text{ACH}_m} = \frac{1}{m}. \tag{3.10}$$

Therefore, ACH in real scale is $1/m$ times smaller than the ACH obtained in the IFMHT-GUT wind tunnel.
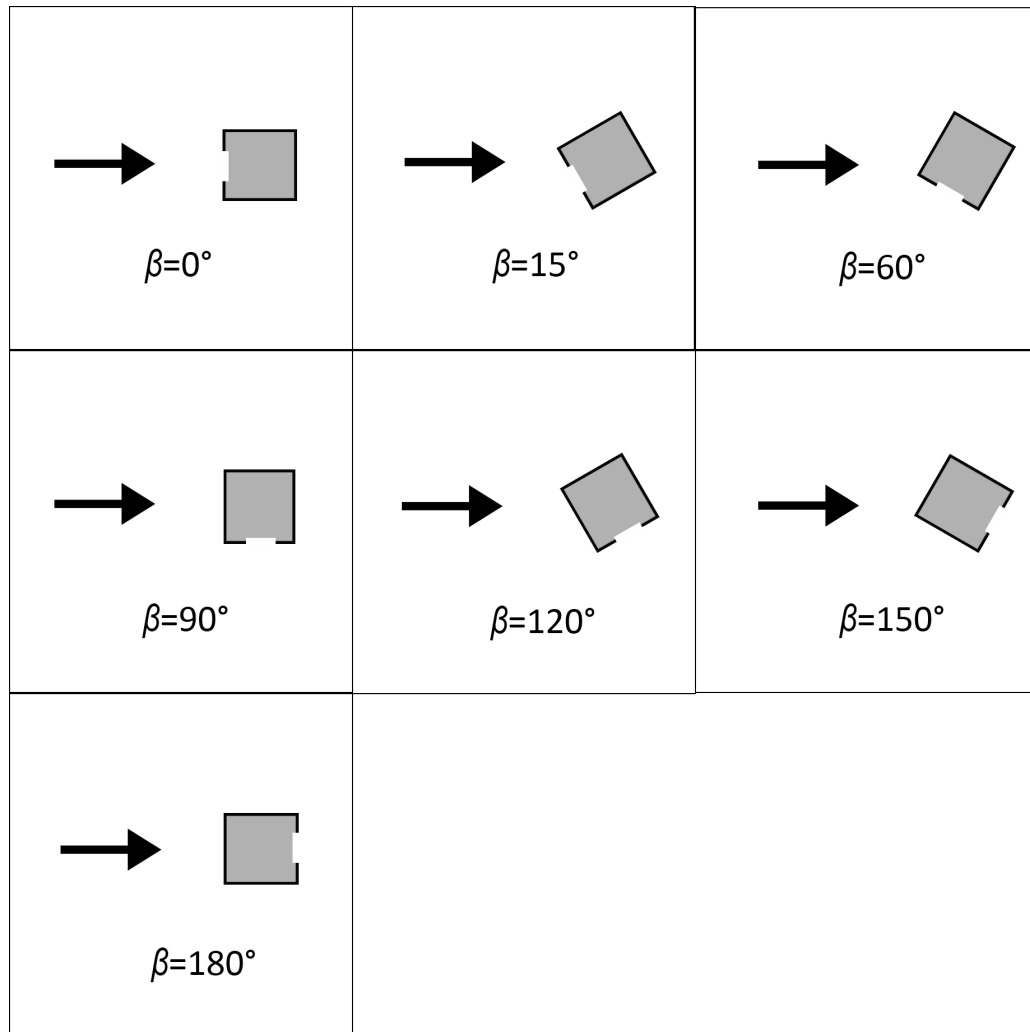
3.5.3 Studied configurations

The air transport through the cubic building model was measured for a stand-alone cubic model first and subsequently for a cubic building model as a part of the urban neighborhood with various spacing densities of buildings. The effects of various flow incidence angles and velocities were studied. Each measurement was carried out for three different velocities (3, 5 and 7 m/s). For all configurations, both cross ventilation and single-side ventilation were investigated.

All studied configurations for a stand-alone cubic building model with two openings (cross ventilation) are presented in Figure 3.19.
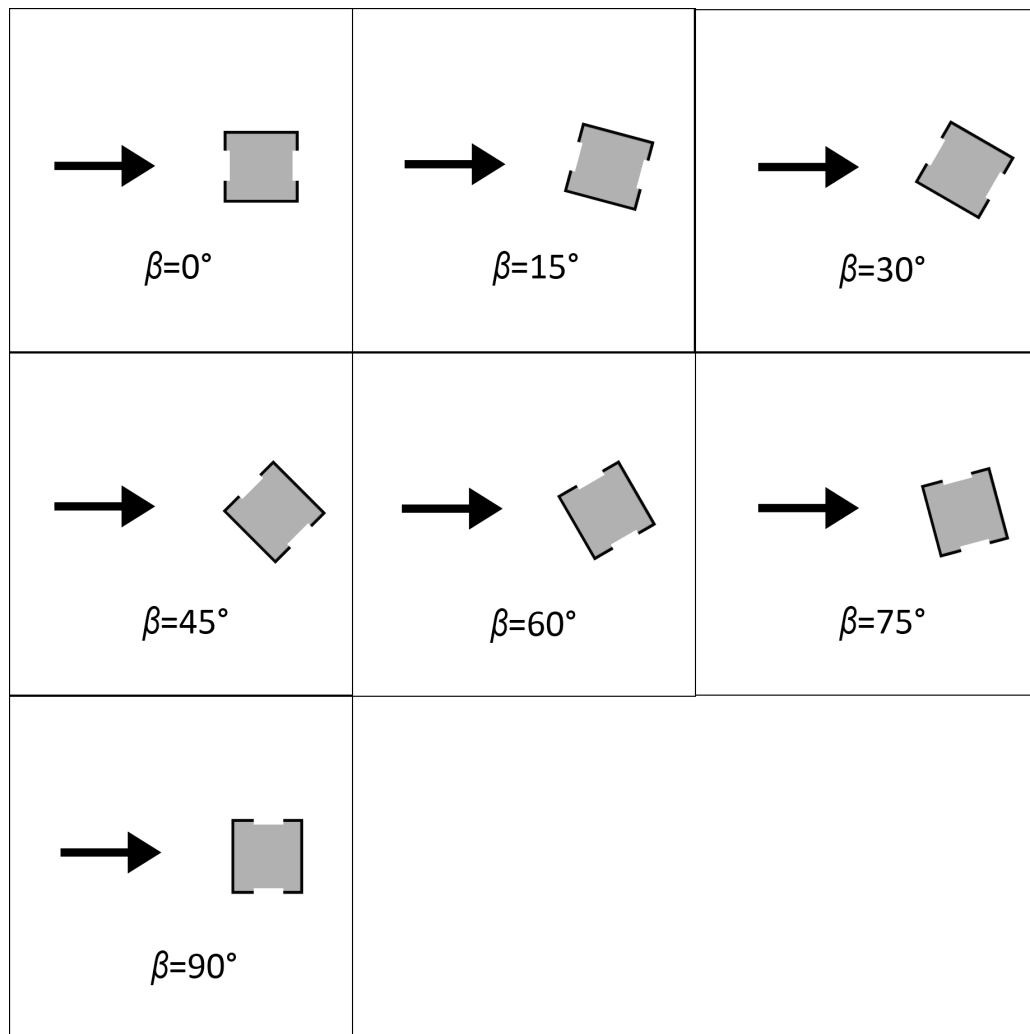
Figure 3.19: Studied configurations for cross ventilation measurements on a stand-alone cubic building model

Figure 3.20 shows configurations for a stand-alone cubic building model with only one opening (single-side ventilation).
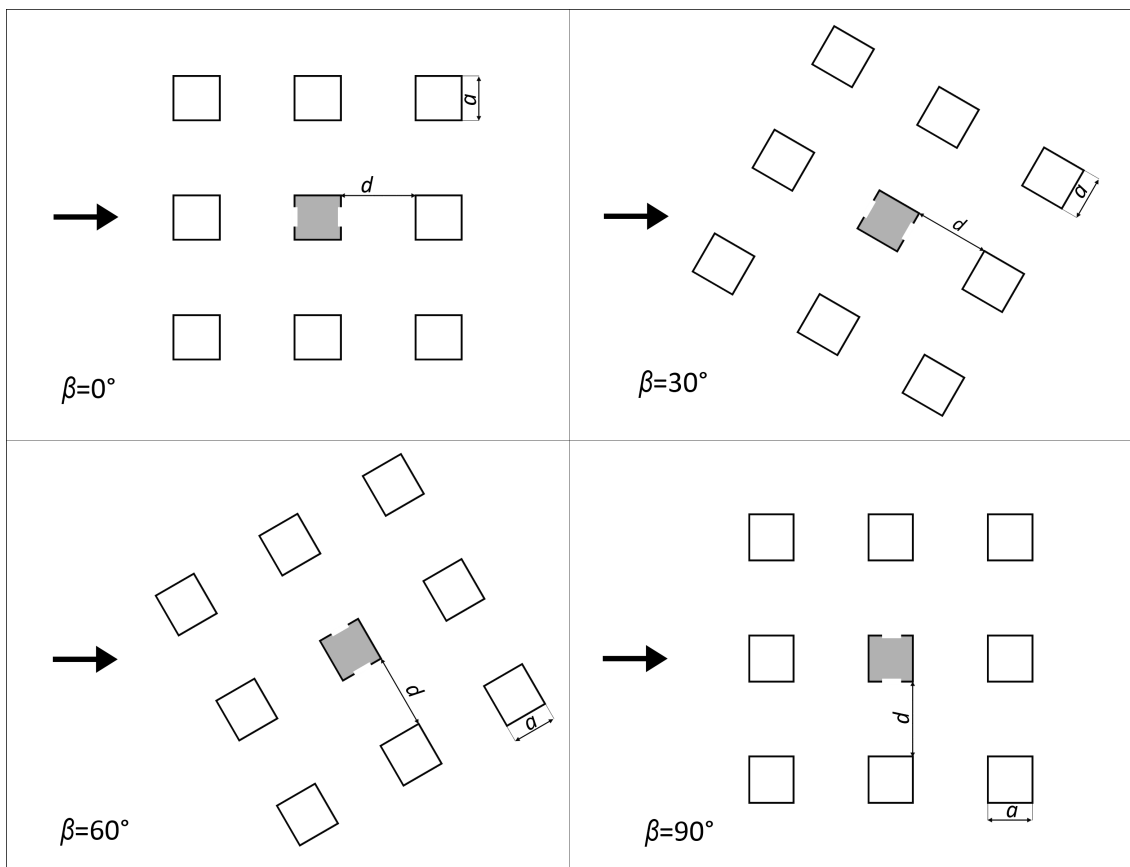
Figure 3.20: Studied configurations for single-side ventilation measurements on a stand-alone cubic building model

For urban-neighborhood tests, eight dummy cubes were placed around the main cubic building model in 3x3 checkered square patterns. Air transport was measured for three different cases:

    a)   Small spacing density of building models, i.e. distance between buildings $d = 100$ mm or $d = 0.5a$, where a is length of an edge of the cubic model ($a = 200$ mm),

    b)   Medium spacing density of building models, i.e. $d = 200$ mm$= a$,

    c)   Large spacing density of building models, i.e. $d = 300$ mm$= 1.5a$.

Configurations for cross ventilation measurements on a cubic building model as a part of the urban neighborhood are shown in Figure 3.21. Single-side configurations are shown in Figure 3.22.

Figure 3.21: Studied configurations for cross ventilation measurements on a cubic building model in an urban neighborhood
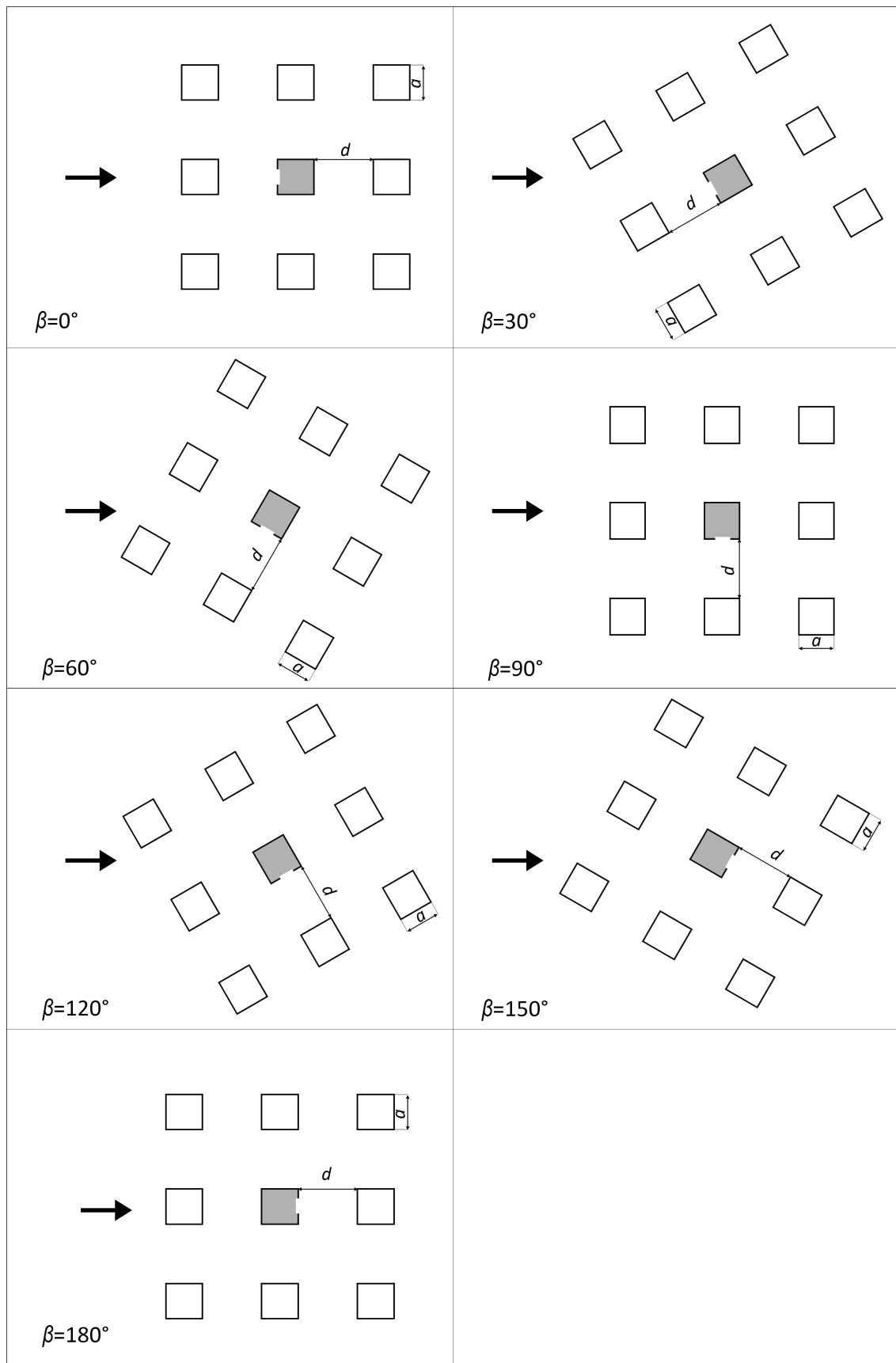
Figure 3.22: Studied configurations for single-side ventilation measurements on a cubic building model in an urban neighborhood

4   Results and discussion

4.1   Atmospheric boundary layer model
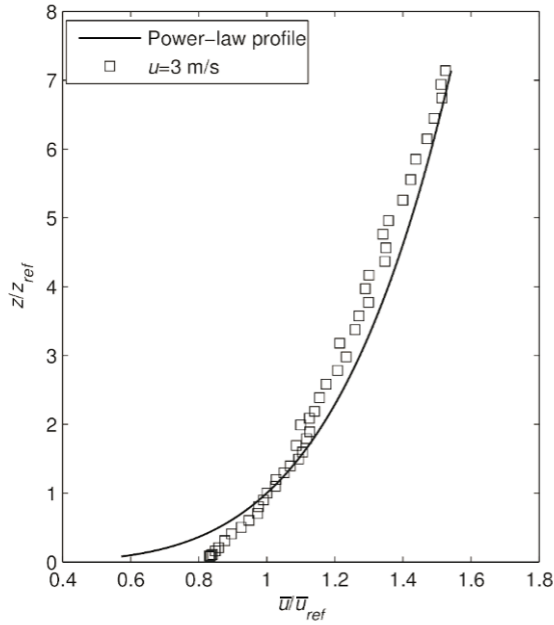
4.1.1   Mean velocity profile

The mean velocity profile was fitted to the power law curve and plotted in a double logarithmic scale to determine the power law exponent α [27], Figure 4.1. Since the power law curve is represented as a straight regression line in double logarithmic plot, its gradient indicates α.
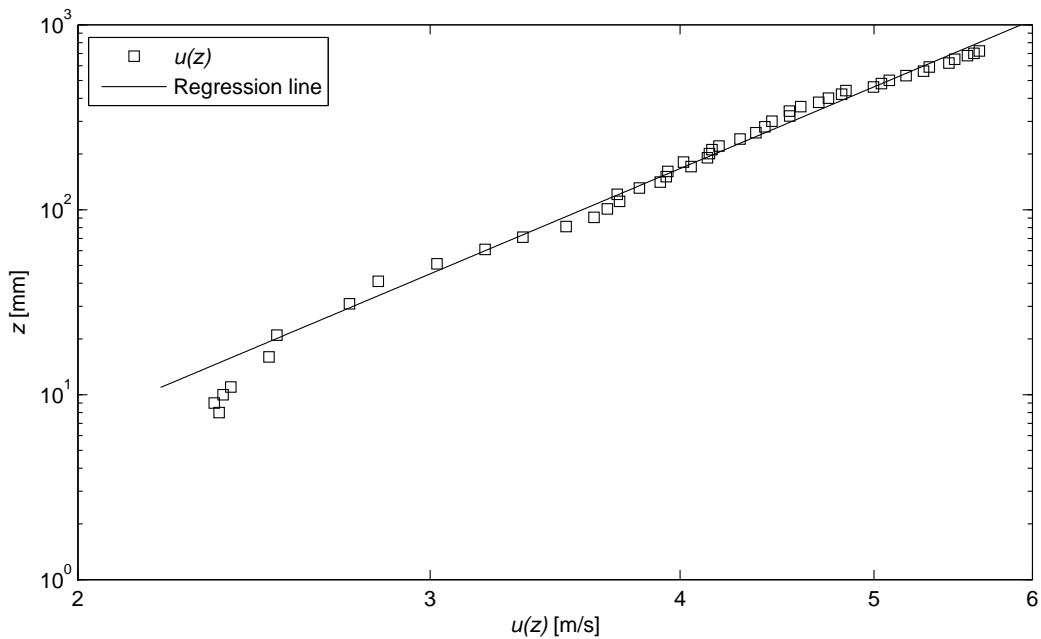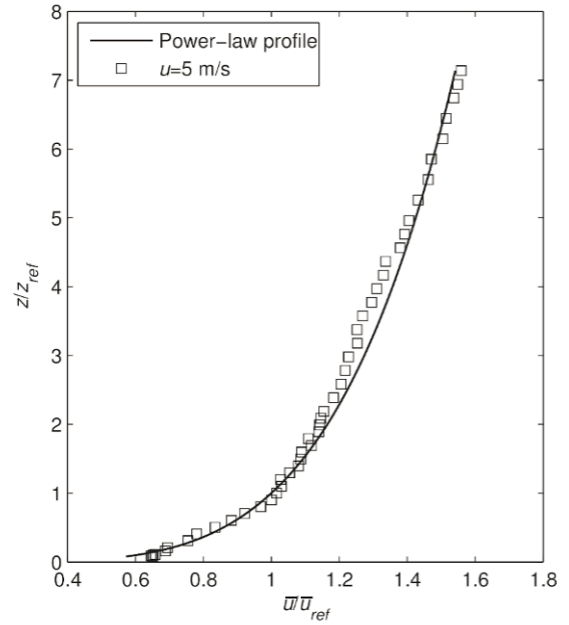

Figure 4.1: Mean velocity profile for *u* = 5 m/s in a logarithmic presentation

An analysis of the fitted regression line yields $\alpha \approx 0.22$, which is commonly adopted to represent the ABL developing above a suburban type terrain. Figure 4.2 shows mean velocity profiles compared to the power-law curve with the power-law exponent $\alpha = 0.22$. The mean velocities at height z were normalized using the reference velocity at $z_{ref} = 100$ mm at the model scale.

A very good agreement with the power law profile can be observed for all the velocities, except for the case with $u = 3$ m/s where experimental data in lower parts deviates from power law profile. This may be due to Reynolds number effects. To check the flow lateral uniformity, the measurements were carried out in the y_C, y_L and y_R planes. Experimental data for all three planes compared to the power law profile is shown in Figure 4.3. The comparison is a clear indication for the lateral uniformity of the flow in the IFMHT-GUT wind tunnel.
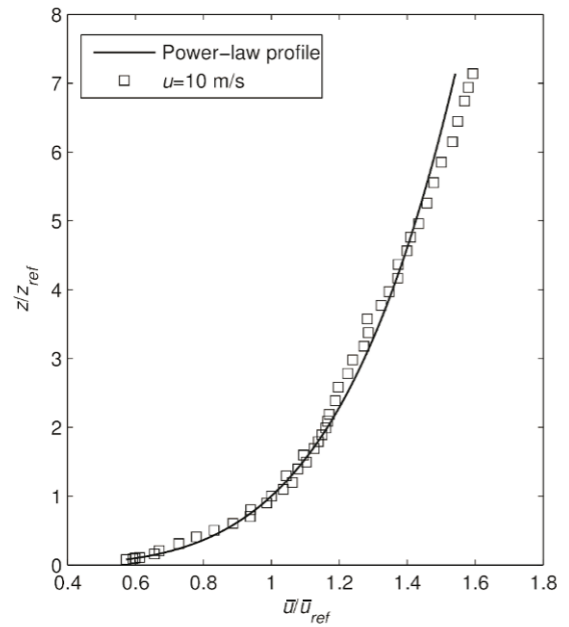
a): *u* = 3 m/s   b): *u* = 5 m/s
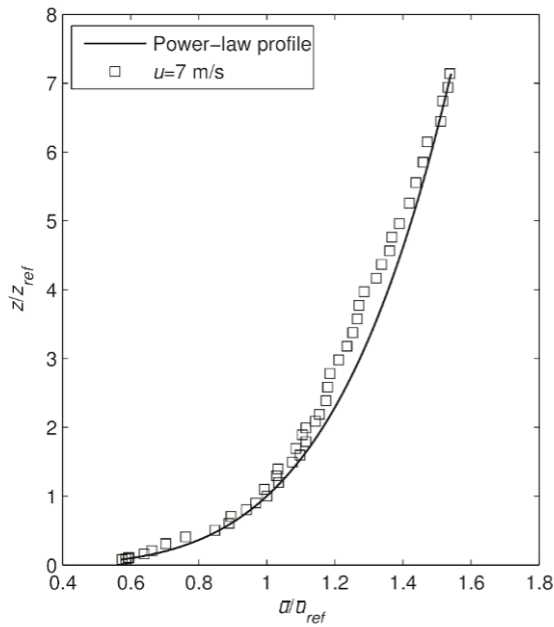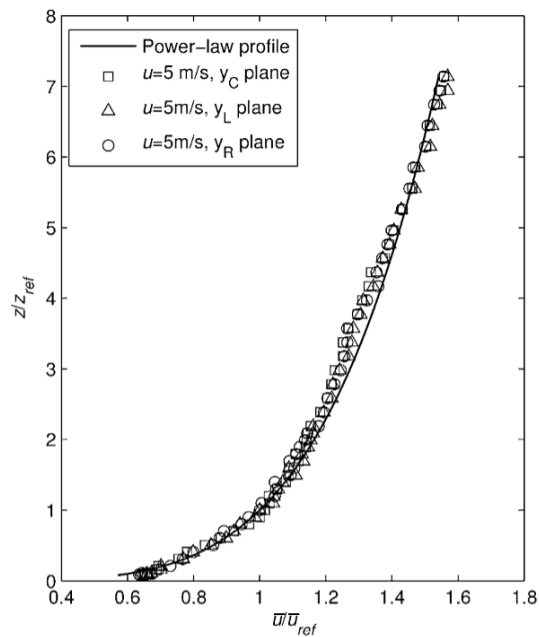
c): *u* = 7 m/s   d): *u* = 10 m/s

Figure 4.2: Mean velocity profiles compared to the power-law profile with $\alpha = 0.22$

Figure 4.3: Mean velocity profiles for u = 5 m/s measured in three different lateral planes (y_C, y_L and y_R) compared to the power-law profile with α = 0.22

According to [27], plotting the results in a semi-logarithmic scale enables to determine the friction velocity u_τ and aerodynamic surface roughness length z_0, Figure 4.4. The inclination of the regression straight line fitted to the experimental data represents u_τ, while the intersection point of the straight line with the y-axis represents z_0.
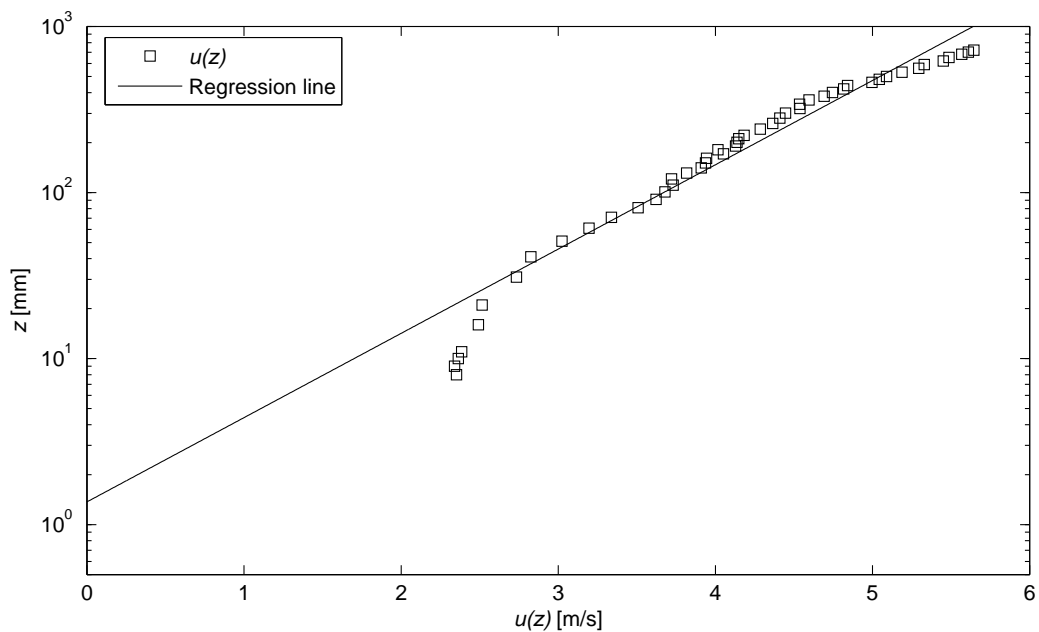
Figure 4.4: Mean velocity profile for u = 5 m/s in a semi-logarithmic presentation

Further analysis yields the aerodynamic surface roughness length $z_{0,m} = 0.00137$ m and friction velocity $u_\tau = 0.35$ m/s. The experimental results compared to the logarithmic profile are shown in Figure 4.5.

a): *u* = 3 m/s   **b): *u* = 5 m/s**

c): *u* = 7 m/s   **d): *u* = 10 m/s**
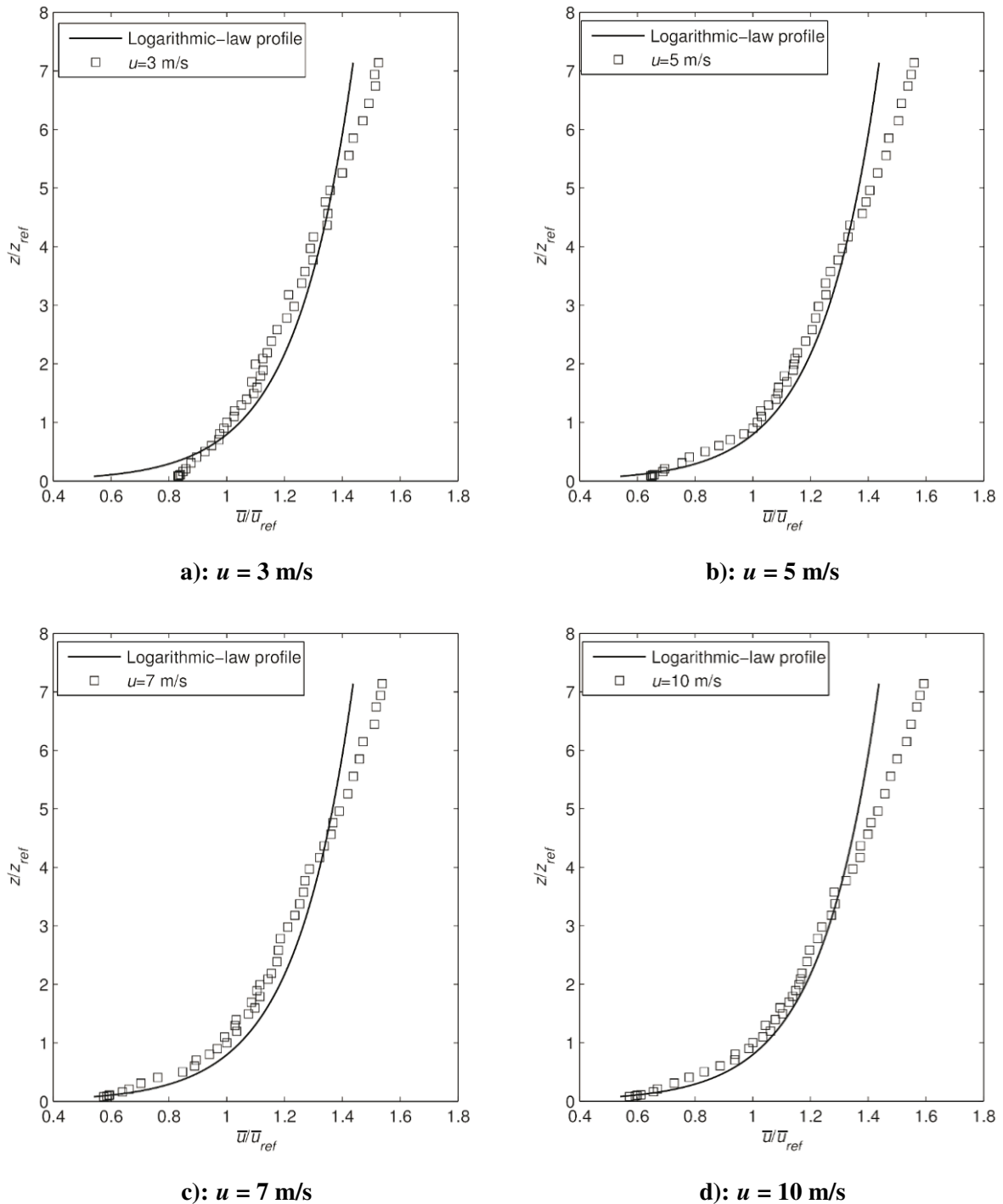
Figure 4.5: Mean velocity profiles compared to the logarithmic law

By comparing Figure 4.2 and Figure 4.5 it can be observed that the experimental results satisfactorily fit the power law, while the results differ more significantly when compared to

the logarithmic law, especially in the upper parts of the ABL simulation.

4.1.2 Simulation length scale factor

The length scale factor was calculated according to [28]:

$$S = \frac{91.3(z-d)^{0.491}}{(L_{u,x})^{1.403}(z_0)^{0.088}}.$$

(4.1)

Scale factors were calculated by applying Eq. (4.1) for each measuring point at increasing heights until the values started to differ significantly. The final length scale factor was determined as an average value of scale factors in single points within the useful height range, [16]. The calculated ABL simulation length scale factor is 1:250.

The determined aerodynamic surface roughness length $z_{0,m} = 0.00137$ in wind tunnel was scaled-up to full-scale using this length scale factor thus yielding $z_{0,p} = 0.34$ m in prototype. This full-scale value of $z_{0,p}$ agrees very well with the ESDU 85020 [1], where aerodynamic roughness lengths $z_{0,p}$ between 0.3 m and 0.5 m indicate suburban terrain, i.e. small towns, suburbs of large towns and cities or wooded country.

4.1.3 Turbulence intensity

The profiles of turbulence intensity in vertical (I_w) and longitudinal (I_u) direction are shown in Figure 4.6 and Figure 4.7, respectively. Furthermore, the I_u results were compared with those of ESDU 85020 [1], where $\pm 25\%$ tolerance margin was used.
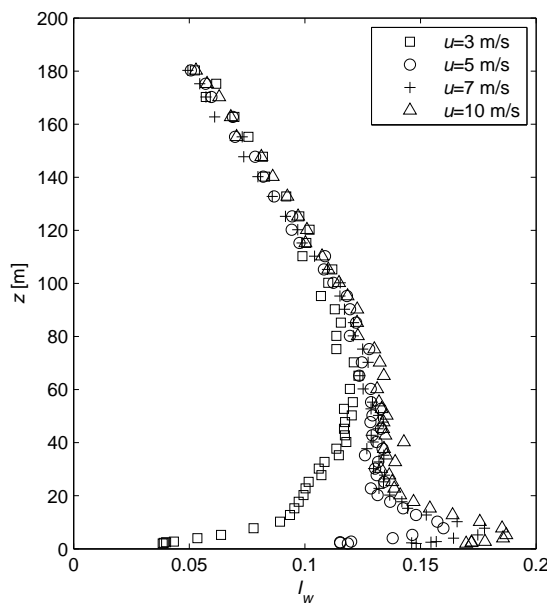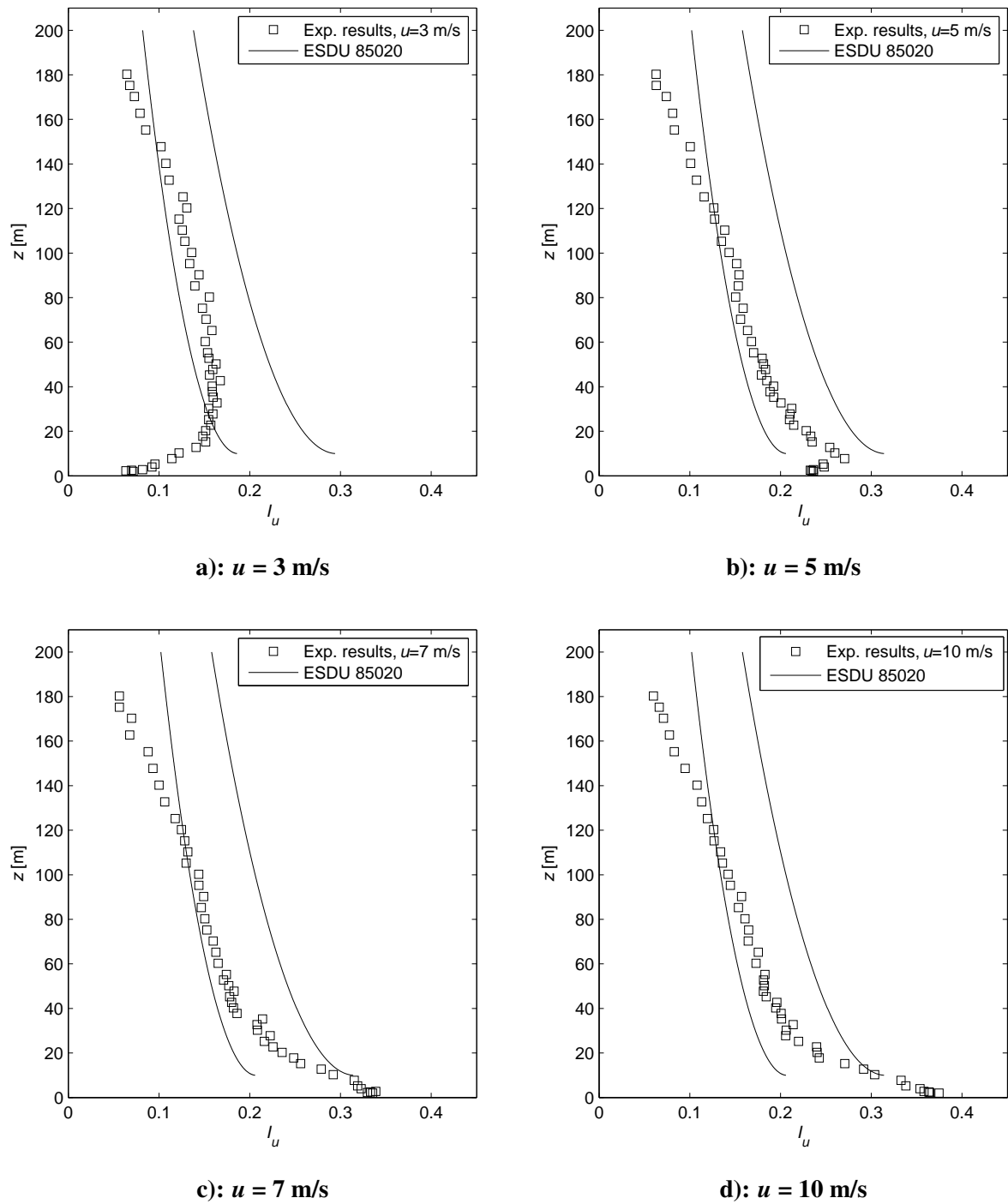

Figure 4.6: Vertical turbulence intensity profiles

a): *u* = 3 m/s   b): *u* = 5 m/s

c): *u* = 7 m/s   d): *u* = 10 m/s

Figure 4.7: Longitudinal turbulence intensity profile compared to ESDU 85020 [1]

The reference velocities applied for calculating turbulence intensities are local mean velocities determined in the measuring point height. The experimental data is closer to the lower margin of the reported ESDU 85020 bandwidth.

4.1.4 Reynolds shear stress

Figure 4.8 presents the obtained Reynolds stress profiles. Reynolds shear stress is normalized using the reference velocity at $z_{ref} = 100$ mm at the model scale. A reasonable consistency of the Reynolds shear stress can be observed within the simulated height of the inertial sublayer.
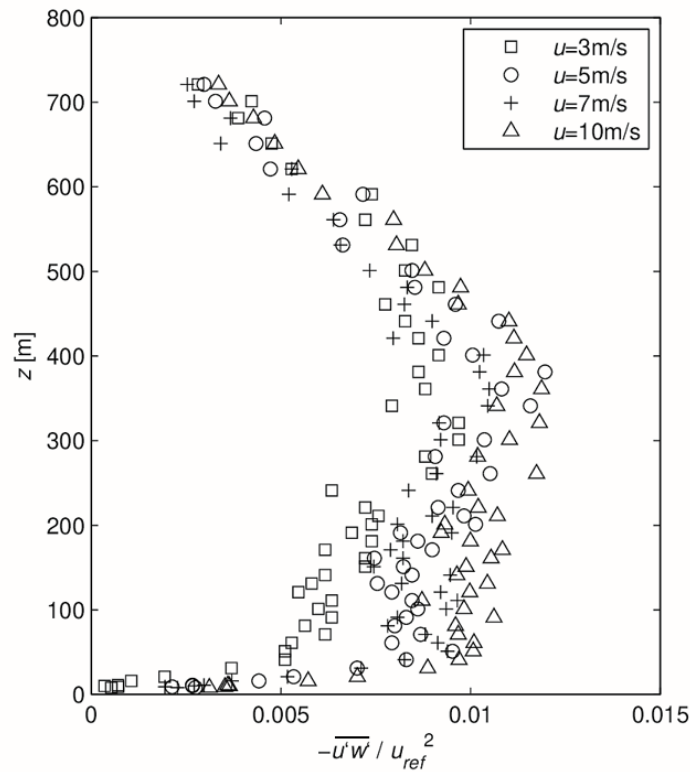

Figure 4.8: Reynolds shear stress

4.1.5 Integral turbulence length scales

Integral turbulence length scales were scaled–up using the simulation length scale factor 1:250 and they are compared to the ESDU 85020 [1], Figure 4.9. Close to surface, the length scales increase with increasing the height. In the upper part of the ABL simulation the length scales remain constant with increasing the height. The reason for this behavior is the fact, that the only limit for creation of large eddies in the nature is Earth's surface, while in the enclosed wind-tunnel test section the bottom surface, the ceiling and the side walls prevent development of large eddies.
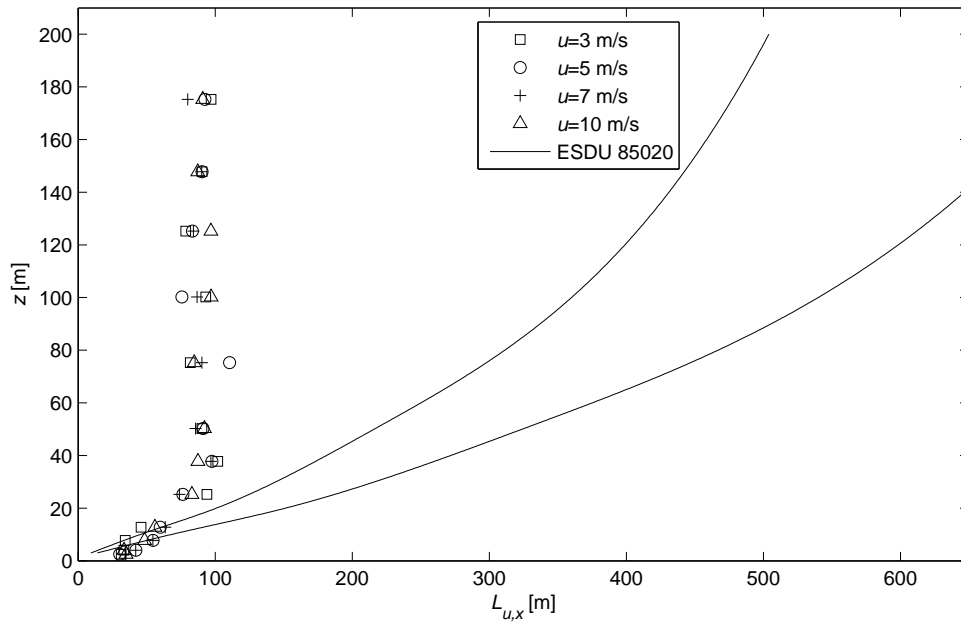
Figure 4.9: Integral turbulence length scales compared to ESDU 85020

4.1.6 Power spectral density of velocity fluctuations

Figures 4.10-4.13 show the power spectral density of longitudinal velocity fluctuations at selected full-scale heights. There is a good match between the measured spectrum and the von Kármán spectrum for the entire frequency range. The presence of a region with a $-2/3$ slope evidently indicates the Kolmogorov inertial subrange.
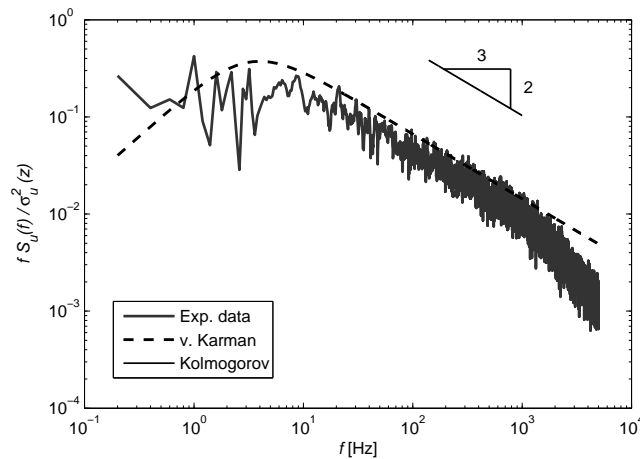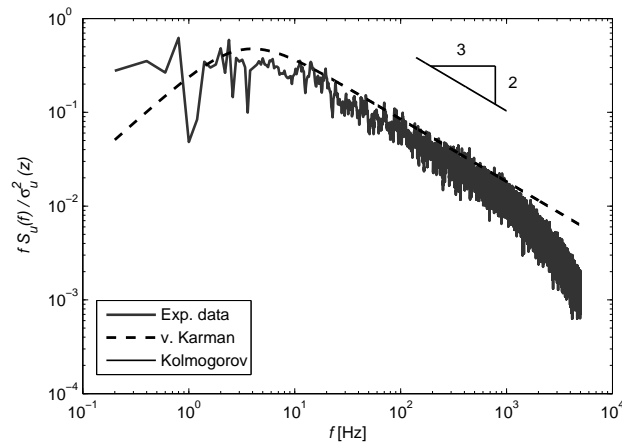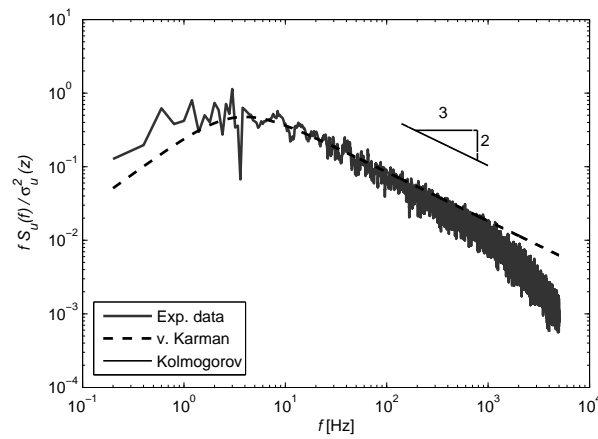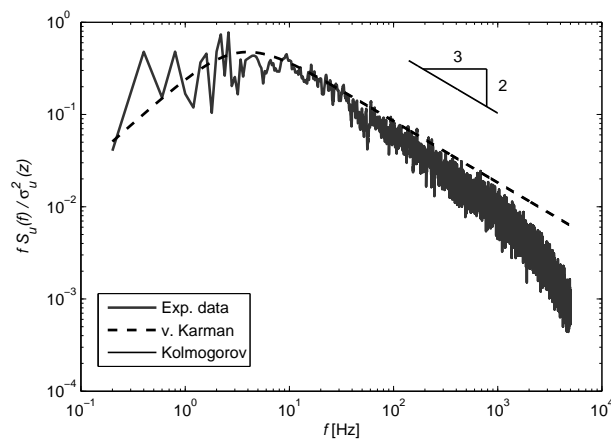

Figure 4.10: Power spectral density of longitudinal velocity fluctuations at z = 5 m compared to Kolmogorov and von Kármán models

Figure 4.11: Power spectral density of longitudinal velocity fluctuations at $z = 15$ m compared to Kolmogorov and von Kármán models

Figure 4.12: Power spectral density of longitudinal velocity fluctuations at $z = 60$ m compared to Kolmogorov and von Kármán models


Figure 4.13: Power spectral density of longitudinal velocity fluctuations at $z = 125$ m compared to Kolmogorov and von Kármán models
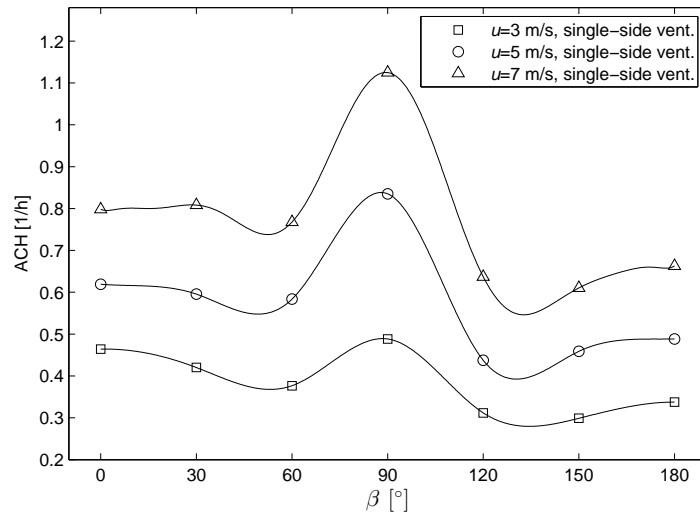
4.2   Building ventilation

4.2.1   Stand-alone building

The air change rates were determined using the tracer gas method by simultaneously measuring concentrations of the used tracer gas in two points. Time intervals were set to 2, 3 and 5 s. The concentration decay method was applied several times for each configuration and the ACH was calculated as an average value of all the measurements. The ACH was subsequently scaled using the simulation length scale factor 1:250. Figure 4.14 and Figure 4.15 show the influence of the flow incidence angle for cross and single-side ventilation on the ACH, respectively.

In the cross-ventilation case, the results show the maximal ACH value at the flow incidence angle $\beta = 0°$. The ACH decreases for an increase in β. At $\beta = 90°$ the ACH reaches the minimum and then, with a further increase in the flow incidence angle, it increases back to its maximal value at $\beta = 180°$, which is due to a symmetry of the cubic building model and its identical position for $0°$ and $180°$, i.e. $\text{ACH}_{0°} = \text{ACH}_{180°}$. On the contrary, for the single-side case, the ACH reaches its peak value at $\beta = 90°$. Referring back to Figure 2.13, the flow separation occurs on cube side surfaces with accompanying suction at the underlying cube surface. In case of $\beta = 90°$, with only one window open on the side, substantially lower outside pressure entrains the mixture out through the opening significantly quicker, which leads to the maximal ACH values. By further comparison of two cases, the ACH values are considerably smaller for a single-side configuration. Thus, for enhancing natural ventilation performance, cross ventilation should be applied whenever possible. The airflow rates are proportional to the flow velocity acting on the model, which is in accordance with previous relevant studies, e.g. [6].
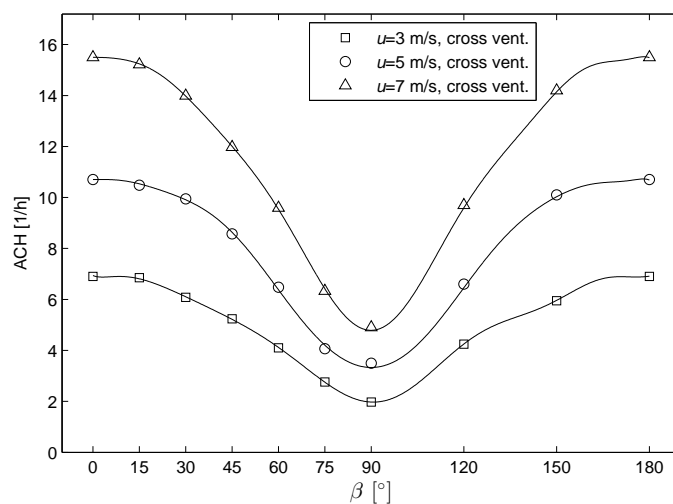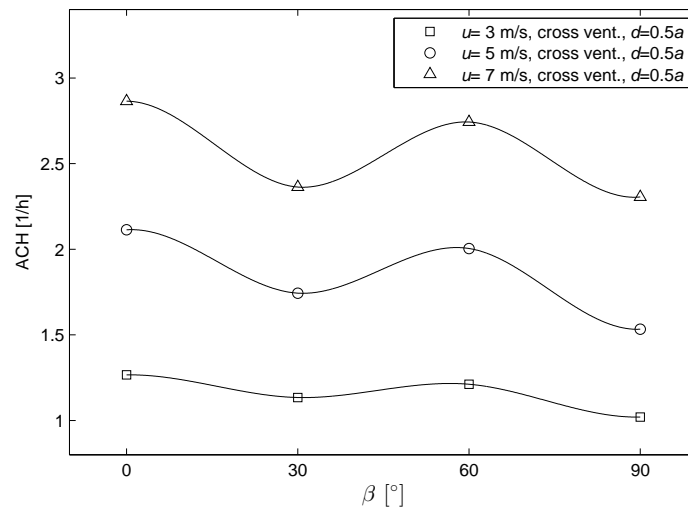

Figure 4.14: Air Change Rate (ACH) for various flow incidence angles for a cross ventilated stand-alone cubic building model

Figure 4.15: Air Change Rate (ACH) for various flow incidence angles for single-side ventilation of a stand-alone cubic building model

4.2.2 Building as a part of the urban neighborhood

Eight dummy cubic building models were used to simulate an urban neighborhood. The cross-ventilation rates were measured for previously described spatial densities (cases a), b) and c) in section 3.5.3), and for various incidence angles β. The obtained ACH rates plotted for various flow incidence angles are shown in Figures 4.16, 4.17 and 4.18.
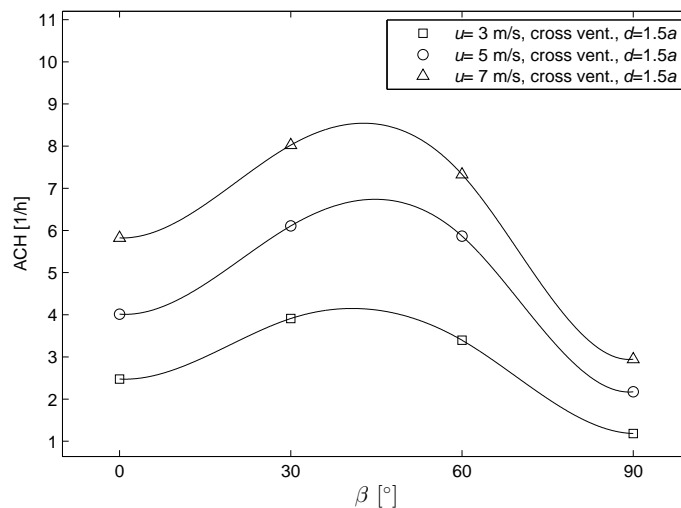

Figure 4.16: Air Change Rate (ACH) for various flow incidence angles for the cubic building model as a part of a group of buildings, cross-ventilation case a)
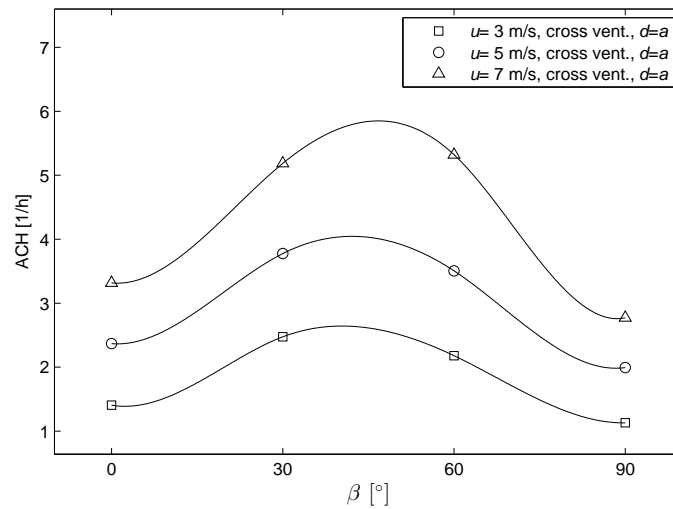
Figure 4.17: Air Change Rate (ACH) for various flow incidence angles for the cubic building model as a part of a group of buildings, cross-ventilation case b)


Figure 4.18: Air Change Rate (ACH) for various flow incidence angles for the cubic building model as a part of a group of buildings, cross-ventilation case c)

It can be observed that different distances between cubic building models in 3 x 3 pattern strongly influence the ACH behavior for various flow incidence angles. For case a), the peak values occur at $\beta = 0°$ and $\beta = 60°$, while the flow incidence angles $\beta = 30°$ and $\beta = 90°$ indicate lowest ACH values. However, for cases b) and c), the ventilation rate at initial position $\beta = 0°$ becomes lower than the ACH obtained at and between incidence angles $\beta = 30°$ and $\beta = 60°$. This is due to the fact, that at certain flow incidence angles, larger passages between buildings (cases b) and c)) enable undisturbed flow to directly pass through the building opening, thus enhancing the ventilation. Figure 4.19 shows two configurations at $\beta = 0°$ and $\beta = 30°$, case b). It can be clearly seen that at $\beta = 30°$ there is a direct flow

through the window, while at $\beta = 0°$ the dummy cubic building model significantly blocks the flow.

a): $\beta = 0°$ b): $\beta = 30°$
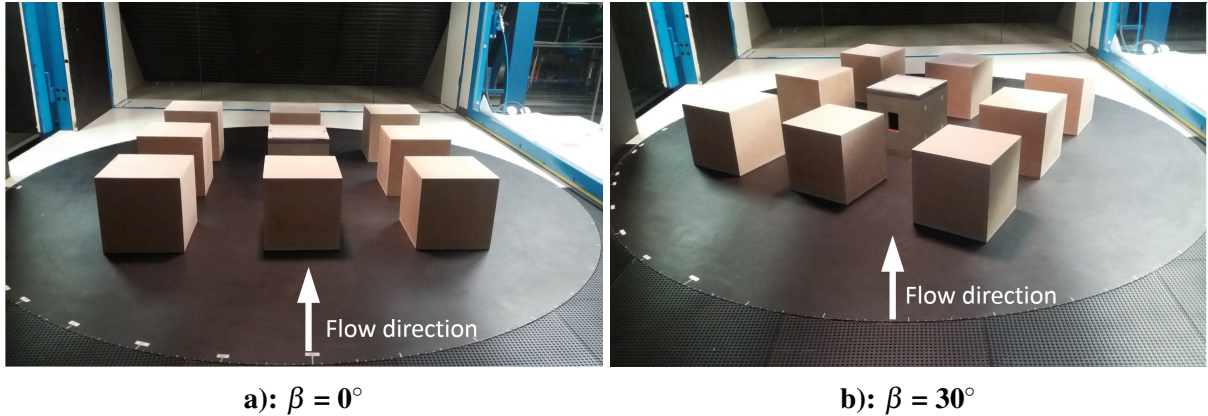
**Figure 4.19: Cubic building models in 3 x 3 square pattern, case b)**

Figures 4.20, 4.21, 4.22 and 4.23 show measured ventilation rates for various spacing densities in urban neighborhood and four selected flow incidence angles. With cubic building models placed farther away from one another (smaller spacing density), the ACH values for cross ventilation consequently increase, which was expected according to Cheung and Liu [11]. Moreover, a significant decrease in the ACH magnitudes can be observed when comparing the results obtained for a cubic building model surrounded by other building models in an urban neighborhood in comparison with the results measured for an isolated stand-alone cubic building model.
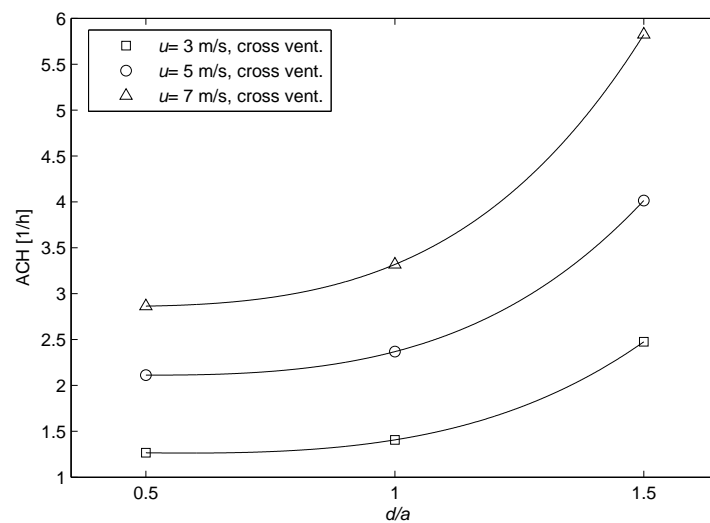
Figure 4.20: Air Change Rate (ACH) for various distances between buildings, cross ventilation, β = 0°
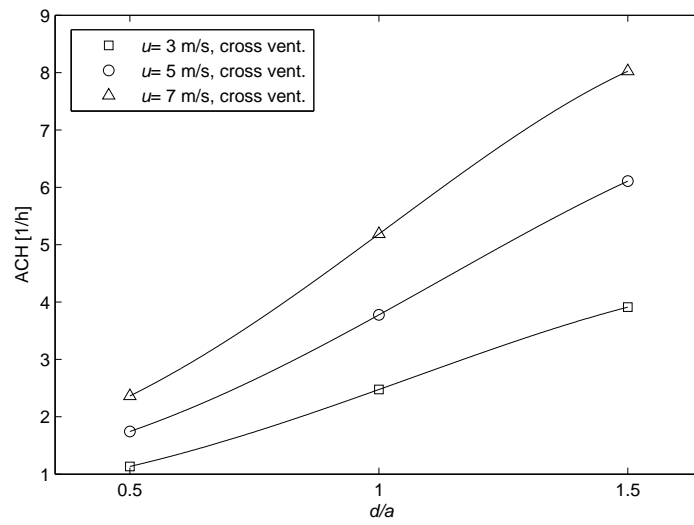
Figure 4.21: Air Change Rate (ACH) for various distances between buildings, cross ventilation, β = 30°
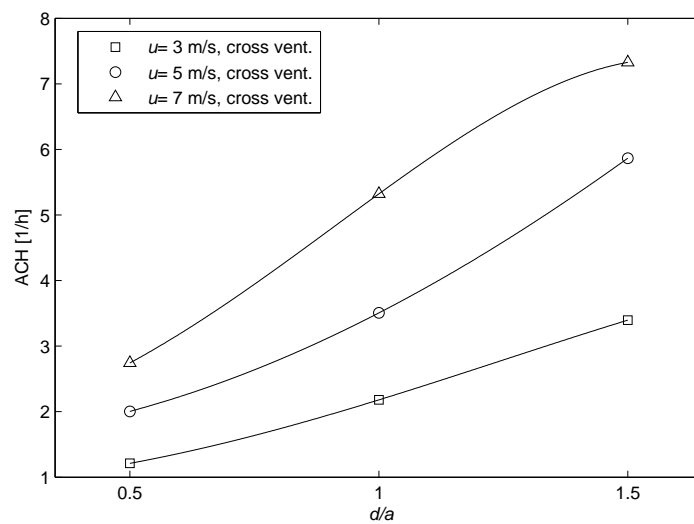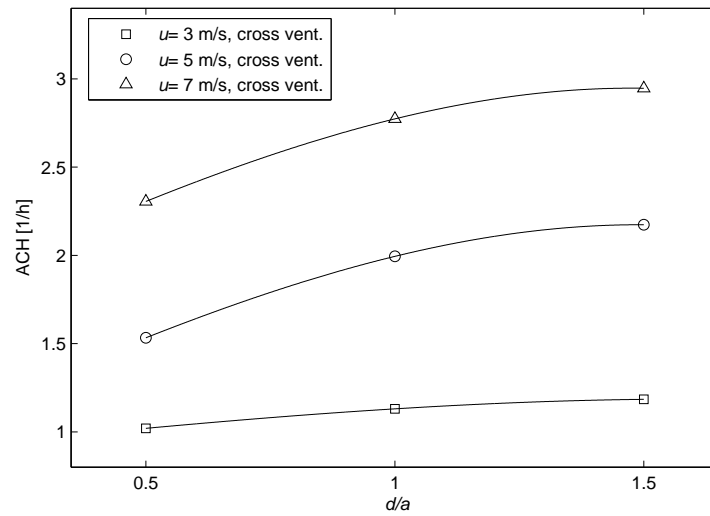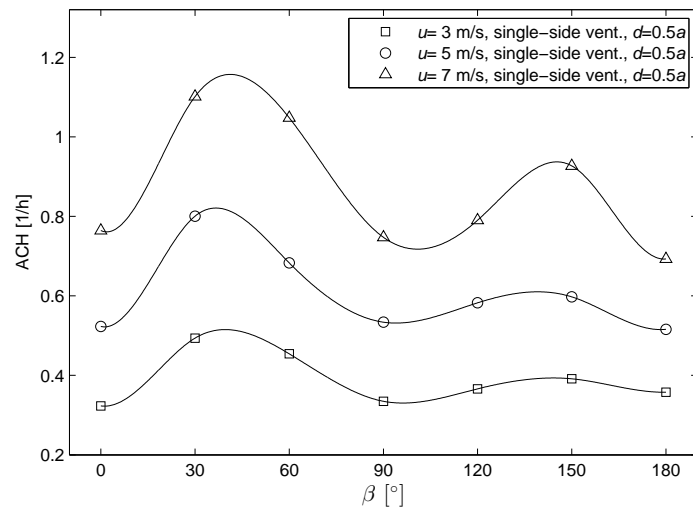

Figure 4.22: Air Change Rate (ACH) for various distances between buildings, cross ventilation, β = 60°

Figure 4.23: Air Change Rate (ACH) for various distances between buildings, cross ventilation, β = 90°

In addition to the cross-ventilation experiments, the single-side ventilation was studied as well. Figures 4.24, 4.25 and 4.26 present measured ACH against various flow directions for a single-side configuration. Since the single-side cubic building model has one plane of symmetry less then the model with two opposing openings, the measurements were carried out in a range of flow incidence angles from $\beta = 0°$ to $\beta = 180°$.

Figure 4.24: Air Change Rate (ACH) for various flow incidence angles for the cubic building model as a part of a group of buildings, single-side ventilation case a)

Figure 4.25: Air Change Rate (ACH) for various flow incidence angles for the cubic building model as a part of a group of buildings, single-side ventilation case b)

Figure 4.26: Air Change Rate (ACH) for various flow incidence angles for the cubic building model as a part of a group of buildings, single-side ventilation case c)

When comparing the results with previous data obtained for a single-side ventilation on stand-alone buildings, Figure 4.15, certain differences may be observed. The maximum ACH values are shifted to the flow incidence angle $30° < \beta < 60°$. The maximal ACH measured when building is a part of the urban neighborhood for cases b) and c) is larger than the maximum rate obtained for a stand-alone cubic building model, thus indicating positive building interference. Potential reason for that is speed-up in airflows in tight passages between the building models, which yields lower pressure at their side surfaces. Due to these suction zones, pressure differences between the inner and outer air are larger, which causes inside air to more effectively move out of the cubic building model. Further data analysis is

conducted by plotting the ventilation rates for different distances between the cubic building models d. Figures 4.27 - 4.33 show dependence of the ACH on the spacing density for seven various flow incidence angles.

Figure 4.27: Air Change Rate (ACH) for various distances between buildings, single-side ventilation, $\beta = 0°$

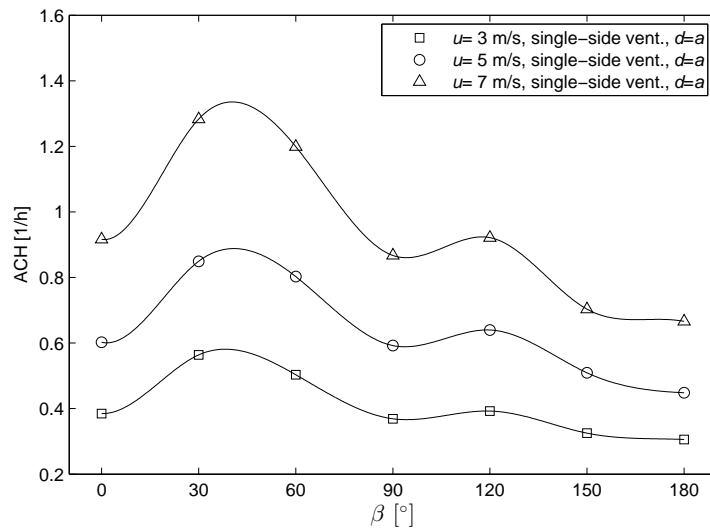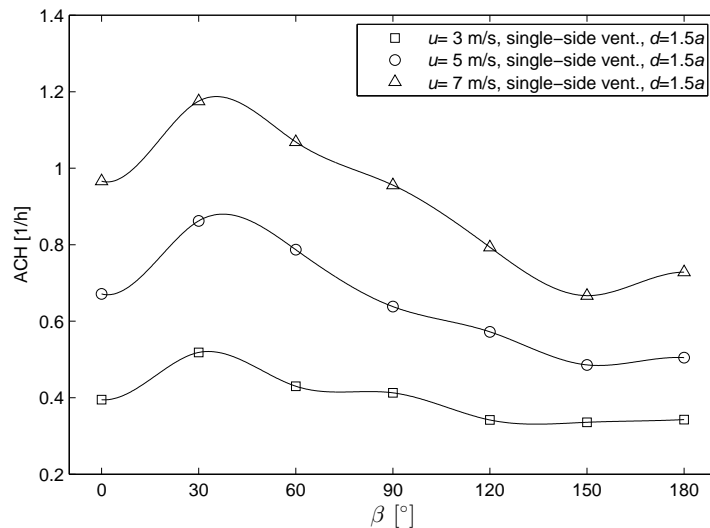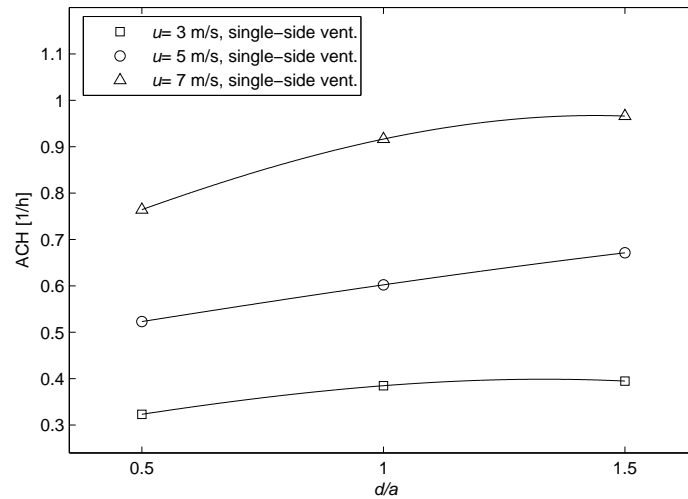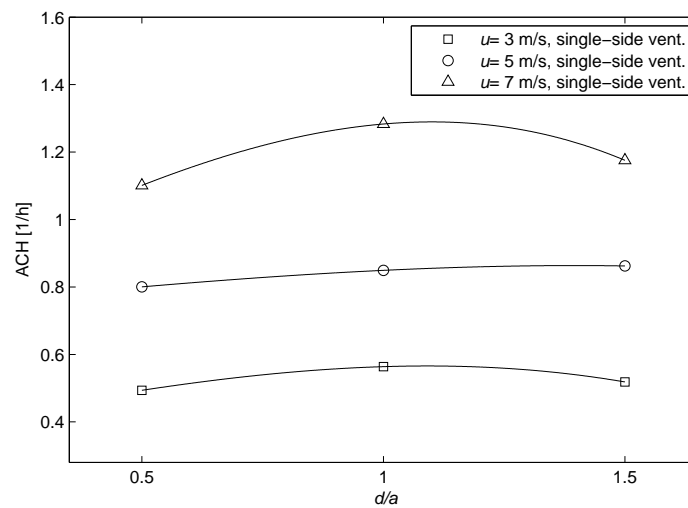**Figure 4.28: Air Change Rate (ACH) for various distances between buildings, single-side ventilation, $\beta = 30°$**

Figure 4.29: Air Change Rate (ACH) for various distances between buildings, single-side ventilation, $\beta = 60°$
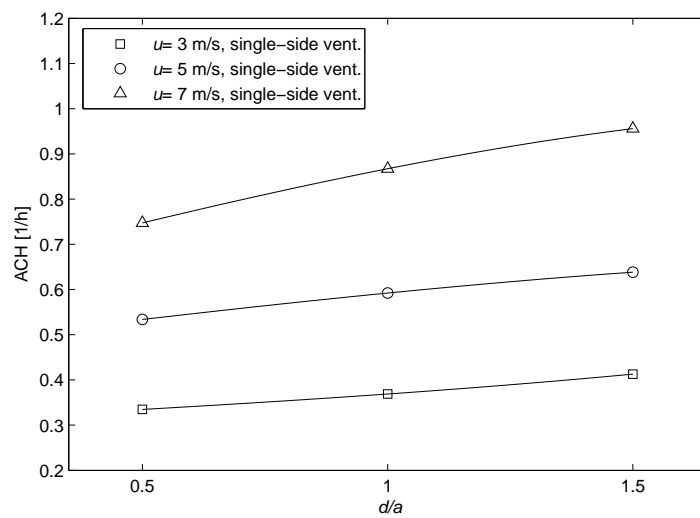
Figure 4.30: Air Change Rate (ACH) for various distances between buildings, single-side ventilation, $\beta = 90°$
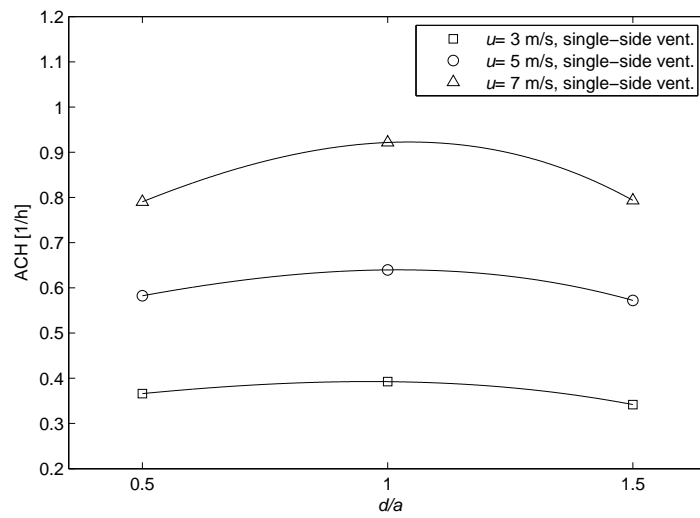
Figure 4.31: Air Change Rate (ACH) for various distances between buildings, single-side ventilation, $\beta = 120°$
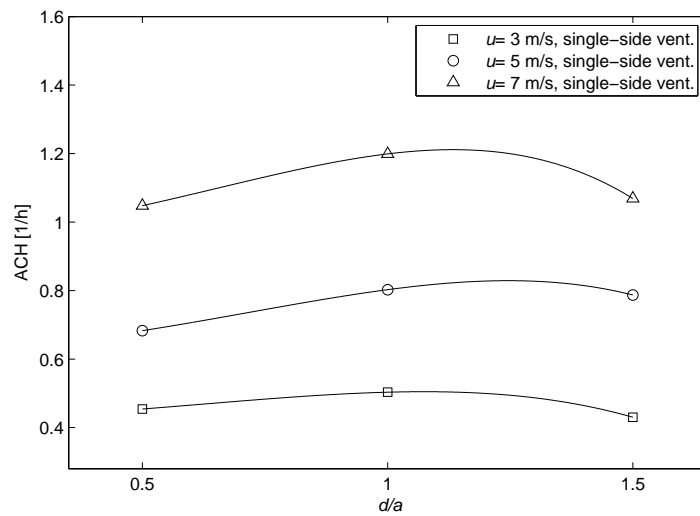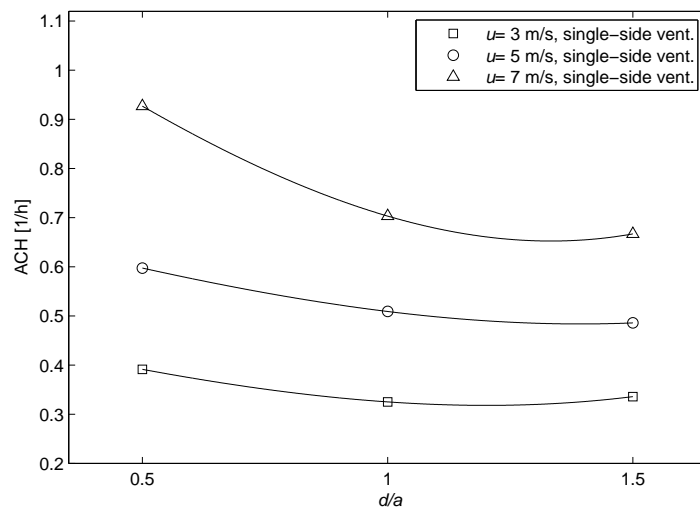

Figure 4.32: Air Change Rate (ACH) for various distances between buildings, single-side ventilation, $\beta = 150°$
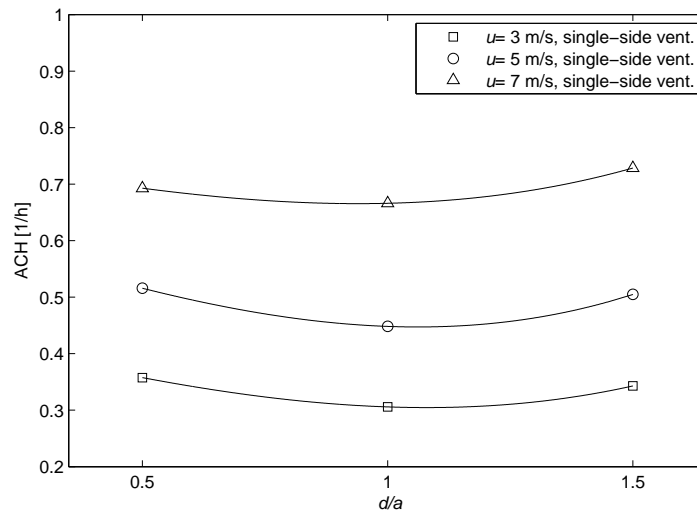
Figure 4.33: Air Change Rate (ACH) for various distances between buildings, single-side ventilation, $\beta = 180°$

For $\beta = 30°$, Figure 4.28, the ACH reaches the optimal value for case b), (i.e $d = a$). For $\beta = 150°$, Figure 4.32, the natural ventilation performance decreases with increasing the distance among the cubic building models. This provides another evidence on the dependence of the natural single-side ventilation on the spacing density in urban neighborhoods that significantly alters for various flow incidence angles.

5 Conclusions

The influence of building spacing density on natural ventilation performance was studied in the atmospheric boundary layer (ABL) wind tunnel at the Institute of Fluid Mechanics and Heat Transfer at the Graz University of Technology, Austria. The flow conditions typical for the suburban-type atmospheric boundary layer were created. Hot-wire anemometry was used to determine velocity and turbulence characteristics in the wind-tunnel test section. The results were reported as profiles of the mean flow velocity, turbulence intensity, Reynolds shear stress, integral turbulence length scales, and power spectral density of longitudinal velocity fluctuations.

The tracer gas measurement technique was used to determine wind-driven air exchange from the cubic building model. The measurements were performed for a stand-alone cubic building model, as well as for a cubic building model as part of the urban neighborhood model for various spacing densities of buildings. The cross ventilation and single-side ventilation types were investigated. Various flow directions and velocities were considered as well.

The mean velocity profiles are in good agreement with the power law for the exponent $\alpha = 0.22$. This represents a good approximation of the suburban ABL conditions. Turbulence intensities compare well with the ESDU 85020 international standard. In the lower part of the ABL, a relatively constant Reynolds shear stress is observed. Integral turbulence length scales agree with ESDU only near the surface. In the upper part of the ABL simulation, due to the enclosed wind-tunnel test section, turbulence length scales become constant, which does not compare well with the full-scale. The power spectral density of longitudinal velocity fluctuations agrees well with the theoretical models of Kolmogorov and von Kármán.

For the cross-ventilation case on a stand-alone cubic building model, the ACH reaches maximum and minimum values at $\beta = 0°$ and $\beta = 90°$, respectively. The airflow rates for single-side ventilation are substantially smaller with peak values observed at $\beta = 90°$, which is due to enhanced suction at the sides of the cubic building model. For the cross-ventilated building model surrounded by other objects, the ACH increases when the spacing density of building models is smaller, i.e. when the building models are placed farther away from each other. However, for a single-side ventilation, an adverse building interference gradually diminishes and with suitable combination of a spacing density among building models and the flow direction, this at the beginning adverse effect eventually becomes favorable for ventilation efficiency.

References

[1] ESDU, Engineering Sciences Data Unit, 85020, "Characteristics of atmospheric turbulence near the ground, Part II: single point data for strong winds (neutral atmosphere)," 1985.

[2] Counihan, J., "Adiabatic atmospheric boundary layers: A review and analysis of data from the period 1880-1972," Atmospheric Environment, 9:871-905, 1975.

[3] Kozmar, H., "Utjecaj mjerila na strukturu modeliranog atmosferskog graničnog sloja," PhD. Thesis, Zagreb, 2005.

[4] Martin A., Fitzsimmons J., "Making Natural Ventilation Work," Bracknell, Berkshire, 2000.

[5] Escombe R., Oeser C., Gilman R., Navincopa M., Ticona E., Pan W., Martinez C., Chacaltana J., "Natural Ventilation for the Prevention of Airborne Contagion," 2007.

[6] Teppner R., Langensteiner B., Meile W., Brenn G., Kerschbaumer S., "Air change rates driven by the flow around and through a building storey with fully open or tilted windows: An experimental and numerical study," Energy and Buildings 76:640–653, 2014.

[7] Schulze T., Eicker U., "Controlled natural ventilation for energy efficient buildings," Energy and Buildings 56:221-232, 2013.

[8] Ernest D., Bauman F., Arens E., "The effects of external wind pressure distributions on wind-induced air motion inside buildings," Journal of Wind Engineering and Industrial Aerodynamics 44:2539-2550, 1992.

[9] Heiselberg P., Svidt K., Nielsen P., "Characteristics of airflow from open windows," Energy and buildings 36:859-869, 1990.

[10] Lee B., Hussain M., Soliman B., "A method for the assessment of the wind induced natural ventilation forces acting on low rise building arrays," Building Services Engineering Research and Technology 1:35–48, 1980.

[11] Cheung O.P., Liu C.H., "CFD simulations of natural ventilation behaviour in high-rise buildings in regular and staggered arrangements at various spacings," Energy and Buildings 43:1149–1158, 2011.

[12] Dyrbye, C., Hansen, S.O., "Wind loads on structures," John Wiley and Sons, London, 1997.

[13] Kaimal, J.C., Finnigan, J.J., "Atmospheric boundary layer flows: their structure and measurement," Oxford University Press, New York, 1994.

[14] Wieringa J., Davenport A., Grimmond C., Oke T., " New revision of Davenport roughness classification. Proceedings of the 3rd European and African Conference on Wind Engineering," Eindhoven, 2001.

[15] Pernpeintner, A., "Lecture notes from course Aerodynamik der Bauwerke," Lehrstuhl für Fluidmechanik, Fakultät für Maschinenwesen, TU-München, 1998.

[16] Kozmar, H., "Scale effects in wind tunnel modeling of an urban atmospheric boundary layer," Theor Appl Climatol 100:153–162, 2010.

[17] Garratt, J.R., "The atmospheric boundary layer," Cambridge University Press, 1994.

[18] Van der Hoven I., "Power spectrum of horizontal wind speed in the frequency range from 0.0007 to 900 cycles per hour," Journal of Meteorology, 1957.

[19] Kozmar, H., "Industrial Aerodynamics (Industrijska aerodinamika)," Material for lectures, 2017.

[20] Martinuzzi R., Tropea C., "Flow around surface-mounted, prismatic obstacles placed in a fully developed channel flow," J Fluids Eng. Trans. ASME, 115: 85–92, 1993.

[21] Baker C.J., "The laminar horseshoe vortex," J. Fluid Mech., 95:347–367, 1978.

[22] Baker C.J., "The turbulent horseshoe vortex," J. Wind Engng Ind. Aerodyn, 6:9–23, 1980.

[23] Langensteiner B., "Transport processes in ventilated buildings," PhD. Thesis, Graz, 2014.

[24] Jorgensen F.E., "How to measure turbulence with hot-wire anemometers - a practical guide," Dantec Dynamics, 2005.

[25] Dantec Dynamics, "Probes for Hot-wire Anemometry, catalogue," 2015.

[26] LumaSense Technologies, "Instruction Manual, INNOVA -1316A-2 Multi Gas Monitor," 2011.

[27] Gromke C., Ruck B., "Die Simulation atmosphärischer Grenzschichten in Windkanälen," Technical report, University of Karlsruhe, 2005.

[28] Cook N.J., "Determination of the model scale factor in wind tunnel simulations of the adiabatic atmospheric boundary layer," Journal of Wind Engineering and Industrial Aerodynamics, 2:311-321, 1978.